



**University of
Nottingham**
UK | CHINA | MALAYSIA

**The Synthesis and Properties of Organic-Inorganic Hybrid
Polyoxometalates Hybridised with Asymmetric
Perylenediimides**

Kai Walters

14314297

Supervised by

Dr Graham Newton

and

Dr Neil Champness

School of Chemistry

University of Nottingham

Contents

Abstract	5
Acknowledgments	6
Colour Scheme	7
Abbreviations	8
1. Introduction	10
<i>1.1 General Polyoxometalate Structure</i>	10
<i>1.2 Keggin and Wells-Dawson Polyoxometalates</i>	12
<i>1.3 Hybridisation of Polyoxometalates</i>	16
<i>1.4 Properties of Polyoxometalates</i>	18
<i>1.4.1 Electronic Properties</i>	18
<i>1.4.2 Optical and Photochemical Properties</i>	19
<i>1.5 Polyoxometalate Catalysis</i>	20
<i>1.6 Photoactive Hybrid Polyoxometalates</i>	22
<i>1.7 Perylene Diimides</i>	25
<i>1.7.1 Introduction to Perylene Diimides</i>	25
<i>1.7.2 Perylene Diimide Structure</i>	26
<i>1.8 Optical and Electronic Properties of Perylene Diimides</i>	26
<i>1.9 Modification of Perylene Diimides</i>	28
2. Aims	30

3. Results and Discussion	31
3.1 <i>Synthesis and Characterisation of Polyoxometalate Precursors</i>	31
3.2 <i>Synthesis and Characterisation of Asymmetric PDI Precursor</i>	35
3.2.1 <i>Synthesis of PTE and PDE</i>	35
3.2.2 <i>Synthesis of PMIDE and PMI</i>	37
3.2.3 <i>Synthesis and Characterisation of PDI</i>	39
3.3 <i>Synthesis and Characterisation of Polyoxometalate Hybrid</i>	44
3.4 <i>Spectroscopic Analysis of the Polyoxometalate Hybrid</i>	50
3.4.1 <i>Infrared Spectroscopy</i>	50
3.4.2 <i>Ultraviolet Visible Spectroscopy</i>	51
3.4.3 <i>Fluorescence Spectroscopy</i>	53
3.5 <i>Electrochemistry</i>	55
4. Conclusions and Future Work	59
5. Experimental	61
5.1 <i>Materials and Instrumentation</i>	61
5.2 <i>Synthesis of Asymmetric PDIs</i>	62
5.2.1 <i>Synthesis of PTE</i>	62
5.2.2 <i>Synthesis of PDE</i>	63
5.2.3 <i>Synthesis of PMIDE</i>	63
5.2.4 <i>Synthesis of PMI</i>	63

5.2.5 Synthesis of PDI-1.....	64
5.2.6 Synthesis of PDI-2.....	64
5.3 Synthesis of Polyoxometalates.....	65
5.3.1 Synthesis of $K_6[P_2W_{18}O_{62}]$ (P₂W₁₈).....	65
5.3.2 Synthesis of $K_{10}[P_2W_{17}O_{61}]$ (P₂W₁₇).....	65
5.3.3 Synthesis of $K_6[P_2W_{17}O_{61}(C_{39}H_{33}N_2O_5P)_2]$ (PDI-POM).....	66
6. Bibliography.....	67

Abstract

In recent years there has been a growing interest in producing sustainable and efficient catalysts. Within this area of research there has been a focus in harnessing solar energy to drive reactions. Polyoxometalates (POMs) have attracted substantial attention in the field of photocatalysis due to their vast structural diversity, inherent redox activity, and photochemical properties. Despite the promising chemical profile of POMs and their potential in photocatalysis, they have been limited by their absorption characteristics which lie almost exclusively within the UV range and show little to no absorption in the visible light region.

Developments in POM chemistry have allowed for new functionalisation strategies to tune the optical, electrochemical and solubility of POM photocatalysts. There has been a growing interest in hybridisation of POMs with photoactive species (chromophores) with the goal of sensitising the POM to visible light and enhance catalytic capacity through intermolecular charge transfer. Perylene diimides (PDIs) have been of particular interest for this purpose due to their excellent absorption and emission profiles and photochemical stability. Asymmetric synthesis approaches have allowed further tweaking of the optical and electronic properties of PDIs and are potentially attractive to complement the properties of POMs forming new visible light driven photocatalysts.

This report describes the synthesis and characterisation of a novel hybrid organic-inorganic POM. Careful consideration has been made into the molecular design of an asymmetric PDI that will impart the best physical and chemical properties to the photocatalytic dyad. The $[P_2W_{17}O_{61}(C_{39}H_{33}N_2O_5P)_2]$ anion was successfully synthesized and characterized by complimentary NMR, mass spectrometry, TGA, IR, UV-vis, fluorescence spectroscopy and electrochemistry. The hybrid POM was successfully synthesised and evidence for favourable intermolecular charge transfer between the PDI and POM components was observed.

Acknowledgments

First and foremost, I would like to express my immense gratitude to my supervisors Dr Graham Newton and Professor Neil Champness for giving me the chance to undertake this project with their amazing groups. You have both offered excellent support and have pushed me to expand my independent research skills and knowledge of chemistry. I sincerely thank you both, it has been a pleasure working in your labs.

I would also like to thank Dr Jamie Cameron for always being my first point of call whenever I needed support and for looking after me over the course of this project. He has continuously taught me how to optimize my reactions and analyse my data, whilst pushing me to deliver to the best of my abilities. Above all else Jamie has always made time for me no matter how big or small the problem and has always given valuable advice and encouragement throughout my project.

I would also like to thank Dr Alex Kibler for offering great scientific advice and continuing to go out of his way to help me throughout my project especially through its most challenging synthetic stages. Likewise, I would like to thank Dr Nic Pearce for being an excellent teacher, introducing me to the world of research chemistry and guiding me through those first few months in the lab. I would also like to thank Dr Sharad Amin, Dr Jack Jordan, Dr Kieran Jones, Nicole Tsang, and the rest of the Newton and Champness groups for all the support, advice, and friendship you have given me over this last year.

Finally, I would like to thank my parents Rhonda and Dean Walters for providing me continued support and encouragement throughout my years of study and the writing of my thesis.

Colour Scheme

Figures not reproduced from the literature adhere to this colour scheme:

Tungsten Light blue

Phosphorus Pink

Oxygen Red

Silicon Orange

Tin Teal

Germanium Brown

Abbreviations

CPS	Counts per second
CV	Cyclic voltammetry
DFT	Density functional theory
DMA	N,N- Dimethylacetamide
DMF	N,N-Dimethylformamide
ESI	Electrospray ionization
Fc ⁺ /Fc	Ferrocenium/Ferrocene
HOMO	Highest occupied molecular orbital
I _p	Peak current
IR	Infra-red
IVCT	Inter valence charge transfer
LMCT	Ligand to metal charge transfer
LUMO	Lowest unoccupied molecular orbital
NMR	Nuclear magnetic resonance
MALDI	Matrix assisted laser desorption/ionisation
MS	Mass Spectrometry
OFET	Organic field effect transistor
OLED	Organic light emitting diode
PDE	Perylene-3,4-anhydride-9,10-dicarbonyl

PDI	Perylene-3,4,9,10-tetracarboxylic Diimide
PMI	Perylene-3,4-imide-9,10-anhydride
PMIDE	Perylene-3,4-dicarboximide-9,10-dicarbonyl
POT	Polyoxotungstate
POM	Polyoxometalate
PPM	Parts per million
PTCDA	Perylene-3,4,9,10-tetracarboxylic dianhydride
PTE	Perylene-3,4,9,10-tetraester
PTSA.H ₂ O	p-Toluenesulfonic acid monohydrate
TEA	Triethylamine
TGA	Thermogravimetric analysis
UV-Vis	Ultraviolet visible

1.Introduction

Polyoxometalates (POMs) are a class of metal oxide clusters formed from early transition metal oxyanions bridged by oxo ligands. POMs are of great interest due to their rich redox, catalytic and photocatalytic activity whilst also having strong thermal and structural stability.^{1,2} Their vast structural diversity as well as their inherent redox and photochemical activity has led to growing interest in using POMs in designing new functional materials.^{3,4} In particular there has been increased development of post synthetic functionalisation methods. These include grafting organic moieties to the POM core, tuning optical and electronic properties or adding new functionalities.^{5,6}

1.1 General Polyoxometalate Structure

POM chemistry encompasses a diverse range of structures. The archetypal POM structures take their names from the researchers who first characterised their crystal structures, Figure 1 gives an overview of the fundamental structures.⁷ The backbone of the POM structure consists of metal atoms often referred to as addenda sites. The addenda atoms are bridged by oxo ligands and form polyhedral $\{MO_x\}$ (M= W, Mo, V etc, X= P, S, Si) units, which act as building blocks for the larger POM structure. The M atom must be able to sustain a high coordination to incorporate the oxo ligands as well as terminal M=O bonds formed via a $d\pi-p\pi$ interaction. To accommodate the high coordination number of these units the M atom requires vacant d orbitals and a suitable sized ionic radius. Typically, M is a group V or VI transition metal in its highest oxidation state, most commonly Mo(VI), W(VI) or V(V).

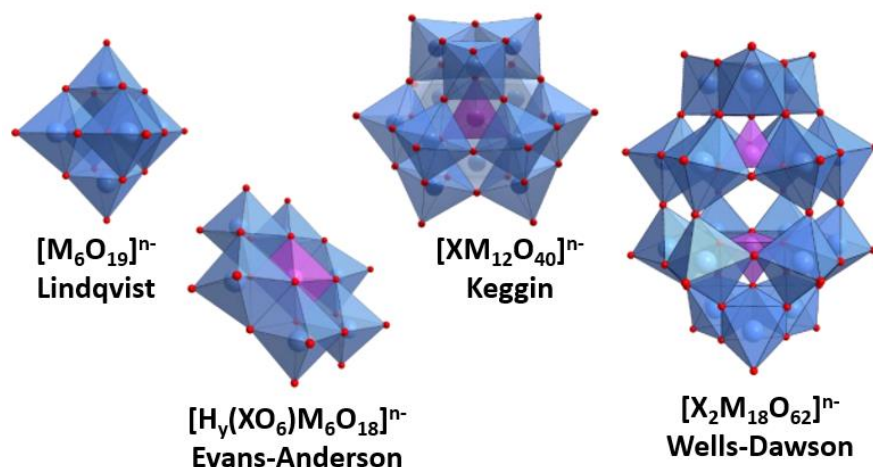


Figure 1: Polyhedra representation of the four archetypal polyoxometalate structures. From left to right: Lindqvist, Evans-Anderson, Keggin and Wells-Dawson. Blue polyhedra: WO_6 , purple: polyhedra PO_4 , red atoms: oxygen.

POMs can be divided into two broad categories based on their general structure. Isopolyoxoanions include POM species whose framework consists exclusively of addenda species, given the general formula $[M_mO_y]^{n-}$. The second category, heteropolyanions, encompass the most explored subset of POMs.^{8,9} Heteropolyanions integrate additional heteroanions into the metal oxide framework with the general formula $[X_xM_mO_y]^{n-}$, where X is usually a p block element most commonly Si(IV), P(V) and S(VI).^{10,11} The incorporation of hetero atoms can be used to template the formation of a wide range of different POM structures. Common examples include four coordinate (tetrahedral) units (e.g., PO_4^{3-} , SO_4^{2-}) found in Keggin and Wells-Dawson structures (described below) and six coordinate (octahedral) units (e.g., $Al(OH)_6^{3-}$) used in Evans-Anderson structures. Figure 2 shows a schematic representation of the self-assembly mechanism of a heteropolyanion POM.

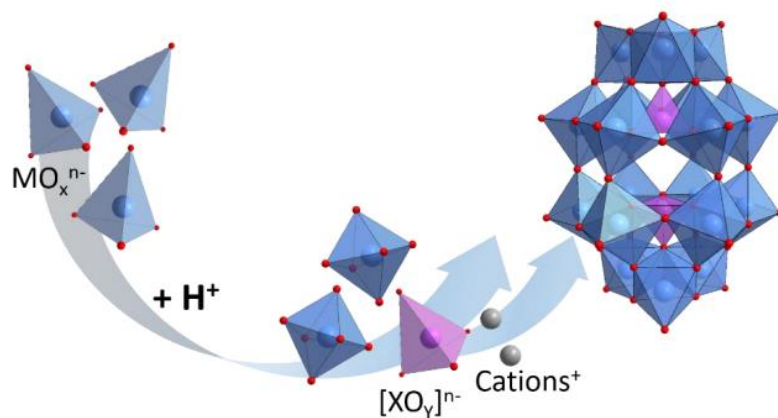


Figure 2: A schematic showing the general condensation pathway of POMs.

1.2 Keggin and Wells-Dawson Polyoxometalates

The Keggin structure consists of octahedral polyhedra where one metal atom is bonded to six oxygens $\{MO_6\}$. Three of these octahedra can assemble into trimetallic groups with shared vertices $\{M_3O_{13}\}$ and the common oxygen site between the three metal centres can link with the template heteroatom $\{XO_4\}$. Consequently, a tetrahedral heteroatom $\{XO_4\}$ can assemble four trimetallic units around it producing the $[XM_{12}O_{40}]$ Keggin structure (Figure 3).

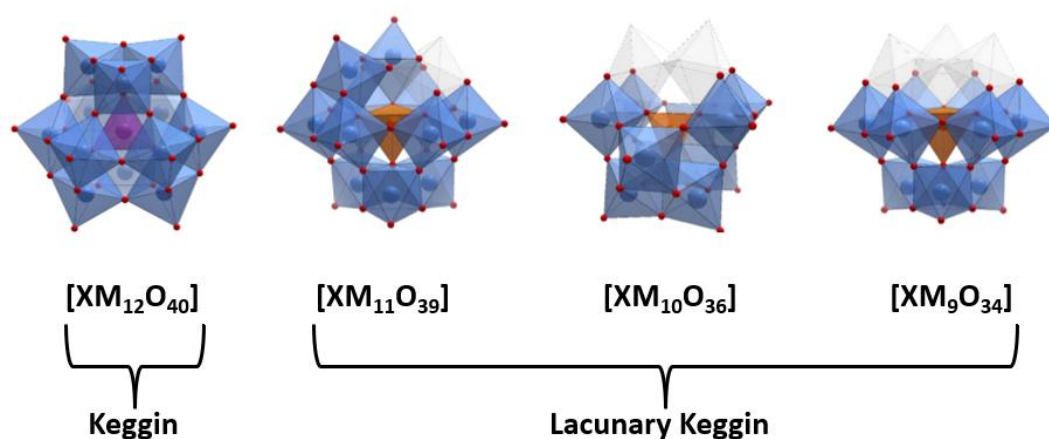


Figure 3: Polyhedra representation of the Keggin structure and three of its lacunary structures. Grey polyhedra represent removed addenda.

The Keggin structure has five isomers produced by rotation of the $\{M_3O_{13}\}$ units through an angle of 60° . Baker and Figgis reported the five isomers, formed by rotating one, two, three or four trimetallic units forming the α , β , γ , δ and ϵ isomers (Figure 4).¹² The changing stability between the isomers can be attributed to increased electrostatic repulsion arising from the change in metal centre distances. Hence, the Keggin isomers follow the stability trend $\alpha > \beta > \gamma > \delta > \epsilon$. Interestingly, reduction of the isomers changes their stability trend with the β isomer becoming the most stable. This is explained by the β isomer having more stable LUMO energies compared to the α isomer upon the second and fourth reductions.

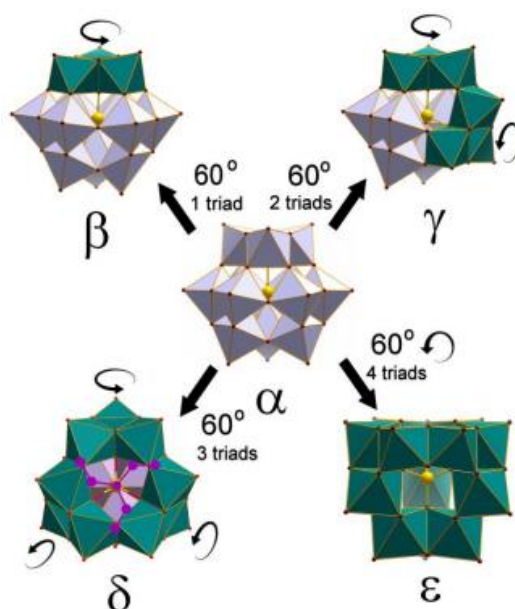


Figure 4: Polyhedra representation of the isomers of the Keggin POM reproduced with permission from ref 13.¹³

The Wells-Dawson POM can be considered a dimer of two lacunary Keggin units $[XM_9O_{34}]$. The resulting POM has two key structural arrangements; trimetallic groups $\{M_3O_{13}\}$ as described in the Keggin structure and bimetallic groups $\{M_2O_{10}\}$ consisting of two metal octahedra with two shared vertices (Figure 5).

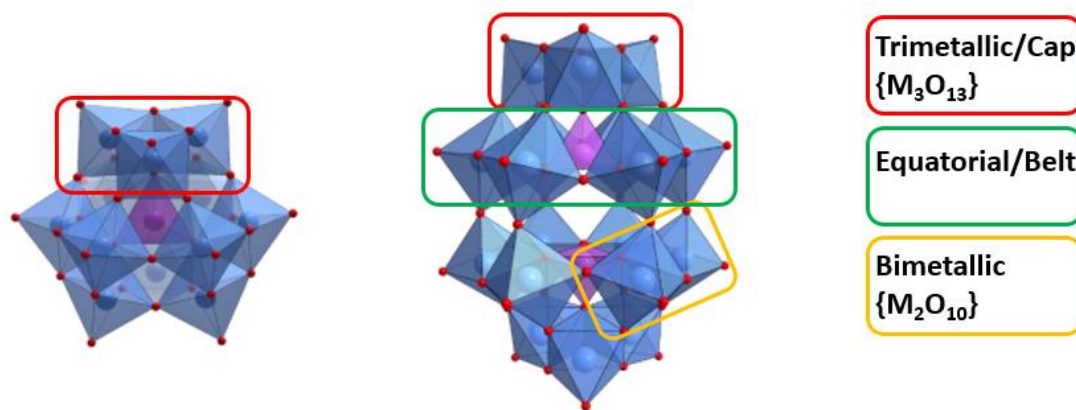


Figure 5: Diagram highlighting the structural motifs of the Keggin and Wells-Dawson POMs. The trimetallic M_3O_{13} caps (red), the belt position (green) and the bimetallic M_2O_{10} units (orange).

As seen with the Keggin structure, each metal group is linked to a heteroatom $\{XO_4\}$ and the two Keggin half units connect to form the Wells-Dawson structure $[X_2M_{18}O_{62}]$ (Figure 6).

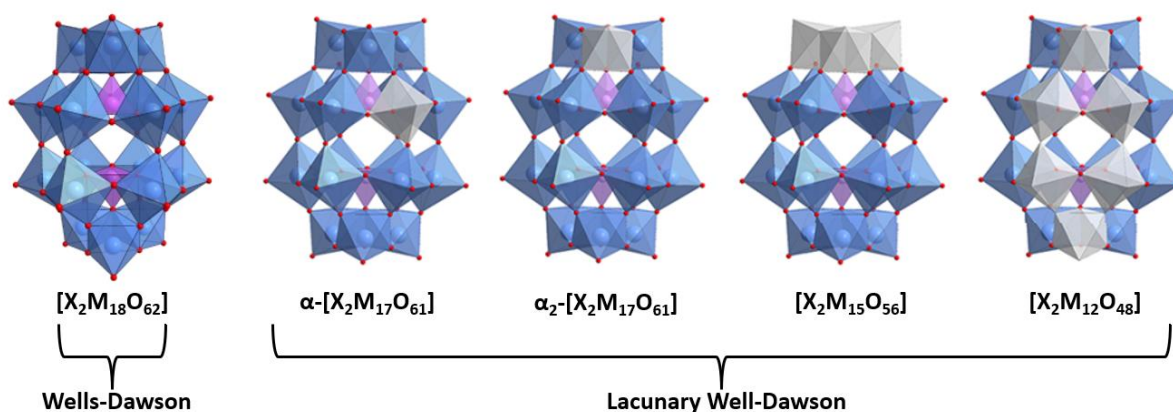


Figure 6: Polyhedra representation of the Wells-Dawson structure and its four possible lacunary structures. Grey polyhedra represent removed addenda.

The addenda atoms are represented by two structural motifs within the Wells-Dawson POM. The two trimetallic units correspond to the apical (cap) positions and the six bimetallic groups are found in the equatorial (belt) position. Several symmetry elements arise as a result of these structural arrangements leading to isomerism. Successive rotations of one or more $\{M_3O_{13}\}$ cap positions through an angle of 60° results in three possible isomers, referred to as α , β and γ isomers (Figure 7).

An additional three isomers can be produced from the α , β and γ isomers by rotating the entire $[XM_9O_{34}]$ half unit through an angle of 60° to form the α^* , β^* and γ^* isomers (Figure 7).^{12, 14} Despite Baker and Figgis postulating the six potential isomers in 1970, only four isomers (α , β , γ , and γ^*) have been isolated. This is explained by the stability trends of the isomers corresponding to tension in the belt position. This is further classified into two categories: eclipsed belt (α , β and γ) and staggered belt (α^* , β^* and γ^*). It has been observed that the former is more stable with a predicted stability trend of $\alpha > \beta > \gamma > \gamma^* > \beta^* > \alpha^*$.¹⁵⁻¹⁸

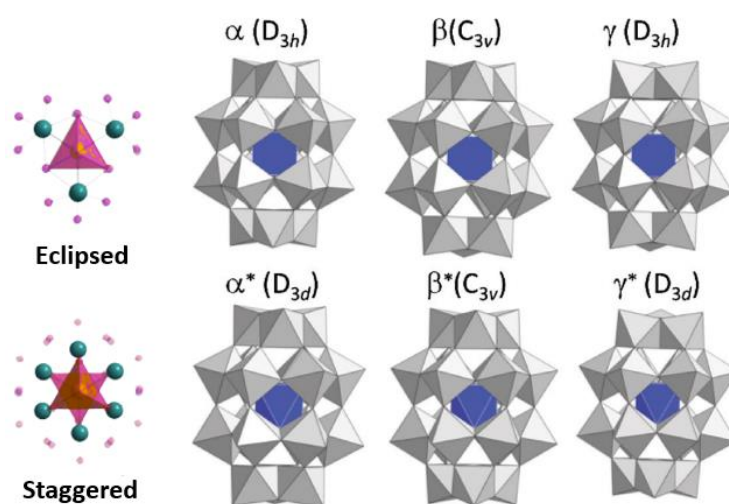


Figure 7: Polyhedra representation of the six Wells-Dawson isomers adapted with permission from ref 19.¹⁹

For post functionalisation of the Wells-Dawson POM it is essential to first form its lacunary structure. As seen with the Keggin structure, lacunary Wells-Dawson structures can be produced by exposing the plenary $[X_2M_{18}O_{62}]$ to alkaline conditions allowing for base catalysed hydrolysis.²⁰ There are three possible lacunary structures formed when either one, three or six addenda clusters are removed. The mono-lacunary ($[X_2M_{17}O_{61}]^{n-}$) Wells-Dawson is formed when one $M=O$ unit is hydrolysed. The mono-lacunary structure also displays isomerism dependent on if the removal of the addenda atoms occurs in the belt or cap region, referred to as the α and α_2 isomers respectively. The tri-lacunary ($[X_2M_{15}O_{56}]^{n-}$

) is formed on removal of three addenda, equivalent to the removal of one cap region. Finally, hydrolysis of six addenda metal centres, the removal of one face of the Wells-Dawson structure, produces the hexa-lacunary Well-Dawson ($[X_2M_{12}O_{48}]^{n-}$). Figure 6 shows a summary of the four lacunary structures that can be obtained from the Well-Dawson POM.

1.3 Hybridisation of Polyoxometalates

The fastest growing area of POM chemistry is post synthetic functionalisation of lacunary POMs. This includes a continuously expanding catalogue of organic-inorganic 'hybrid polyoxometalates', where POM clusters are associated with new ligands or cations. The ability to fine tune physical and electronic properties or introduce new functionalities to a POM has been of particular interest.^{1, 21, 22}

Hybrid POMs can be divided into two categories based on the interaction between the organic and inorganic moieties.⁵ Class I refers to POMs that have non-covalent interactions between the subunits (e.g., hydrogen bonds, van der Waals or electrostatic interactions). The anionic nature of POMs allows for their linkage with organic counter cations to form class I hybrids.²³ Class II hybrids have organic subunits covalently grafted onto the POM. The exposed oxygen centres of lacunary POMs are highly nucleophilic and covalent linkages can be formed by reaction with a range of compatible electrophiles.

Covalent attachment of an organic moiety requires an anchorage point and the conventional route of synthesis forms a M-O-X linkage where X is an electrophilic p block element, these include but are not limited to Si, P and Sn.^{5, 24} Mono lacunary Keggin and Wells-Dawson structures expose four oxygen sites on the lacunas' surfaces, each accessible for further reaction with organic components. The oxygens sit in a distorted square geometry, this topology determines which anchorage groups are most suitable for functionalisation.

Mono functionalisation can be achieved using a M-O-X linker with connections to four oxygen sites, implying that the p-block element must be able to accommodate a high coordination. Primarily organo-stannates and organo-germanates have been used to achieve mono functionalisation.²⁵⁻²⁷ Di-functionalisation of lacuna results from two linkers each connected to two oxygen sites. The lower

coordination is suited to organo-phosphates, organo-arsonates and organo-silicates (Figure 8). Polyoxotungstates (POTs) have primarily been reported in the literature for use in hybrid materials. Lacunary POMs are metastable and are subject to decomposition or isomerization reactions. In particular lacunary polyoxomolybdates and polyoxovanadates have been difficult to isolate, due to rapid decomposition or equilibration preventing isolation and purification.²⁸ In comparison, POTs have greater stability in their lacunary structures, offering a more reliable route for formation of hybrids.²⁹

30

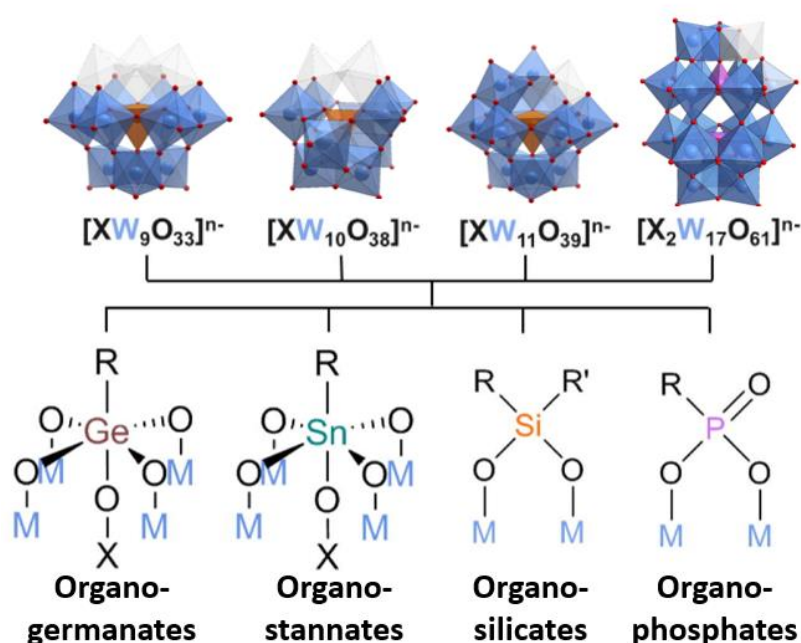


Figure 8: Schematic summary of the key organic linkers for covalent functionalization of lacunary Polyoxotungstates. Adapted with permission from ref 27.²⁷

Several key studies have explored the changes in redox properties and intermolecular charge transfer of POMs. These experiments have shown important consideration should be made to the type of linker and the chain length between the POM and ligand. The type of atom in the linker was examined by Boujtita et al. The group tested the electrochemical properties of two hybrid species, one bearing a silicon linker and the other a phosphorus. Whilst the silicon hybrid had little to no change on redox potential, the hybrid with the phosphorus linker exhibited a positive shift in its first and second redox

processes. The significant shift of 300 mV and 100 mV was attributed to the electron withdrawing character of the phosphonate group.³¹ Subsequent work produced by Harriman et al. explored the importance of linker flexibility and the effect of the ligand conjoined with the POM on its redox properties. The study was able to prove that a flexible linker facilitated intermolecular charge transfer. Conjugation between the ligand and POM was also explored, where full conjugation produced a greater shift in redox potentials compared to the non-conjugated species. The work undertaken by the group showed that suitable ligand choice and careful consideration to the linkers structure can significantly affect the redox properties of the hybrid material.³² The diversity in organic moieties and linkers available has allowed for development of a continuously growing catalogue of organofunctionalized POMs. This offers the potential for higher order structures and refinement of the photo and electrochemical properties of new hybrids.

1.4 Properties of Polyoxometalates

1.4.1 Electronic Properties

Further classification of POMs can be derived from the number of terminal M=O bonds on each octahedral addenda metal unit.³³ One M=O bond (mono-oxo) or two M=O bonds (cis-dioxo) are referred to as Type I and Type II POMs respectively, mixed M=O addenda species are referred to as Type III and are usually formed from lacunary structures. The electronic character of Type I and Type II POMs can be rationalised by considering their molecular orbital arrangement. The octahedral arrangement of the metal centres with either one or two terminal oxygen atoms is electronically analogous to MO_5 and MO_2L_4 species and can be used to understand their redox behaviour. A Type I POM cluster exhibits an idealised local symmetry of C_{4v} where the d-orbitals transform as $a_1 (z^2)$, $b_1 (x^2 - y^2)$, $b_2 (xy)$, and $e (xz, yz)$ (Figure 9).³³ From the diagram we can see a_1 and b_1 are the σ anti-bonding orbitals and e^* is the π anti-bonding component of the terminal oxo bond. The b_2 orbital is formally non-bonding, however shows some anti-bonding character if the equatorial ligand has π interactions with metal centre. This explains how population of the b_2 orbital by one or two electrons will have no

overall effect to the metal ligand bond order. The range of known MOL_5 complexes with d^1 or d^2 metal centres further confirms this theory. Overall, this supports the idea that Type I species can undergo reversible reductions to form isostructural species. The introduction of a second terminal oxo ligand involves the former d_{xy} orbital in the π antibonding structure, hence the cis-dioxo species lack a non-bonding d orbital. Therefore, reduction of Type II POMs populates antibonding orbitals, causing irreversible reduction leading to structural rearrangement or disassembly. This is further supported by the absence of known cis-dioxo d^1 complexes. Hence the most diverse electronic character is displayed by Type I and Type III complexes and have provided the most interesting areas of research.

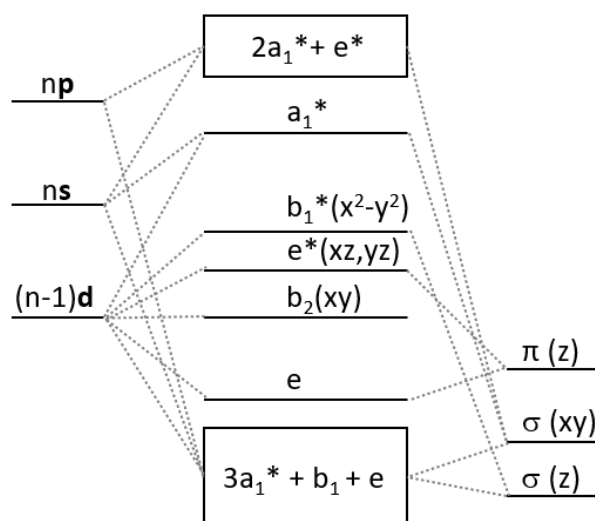


Figure 9: Schematic molecular orbital diagram for MOL_5 complexes of C_{4v} symmetry. Reproduced with permission from ref 33

1.4.2 Optical and Photochemical Properties

Two principal absorption features are displayed by POMs in the ultraviolet-visible (UV-vis) and near infra-red (IR) regions. POMs display strong absorption of UV light (<450 nm) with large extinction coefficients ($\epsilon > 1 \times 10^4 \text{ M}^{-1} \text{ L}^{-1}$) attributed to the ligand to metal charge transfer (LMCT) from the $\text{O} \rightarrow \text{M}$ transition.³⁴ Multiple electron reductions in the $[\text{XM}_{12}\text{O}_{40}]$ (Keggin) and $[\text{XM}_{18}\text{O}_{62}]$ (Wells-Dawson) result in mixed valence species. This gives rise to characteristic inter valence charge transfer

(IVCT) in the range 600-1200 nm and is observed when electrons rapidly migrate between metal centres with thermal assistance. Typically, this absorption occurs at ~700 nm resulting in a distinctive blue colour, hence the species are referred to as the heteropoly blues.^{35, 36} Within Keggin species rapid delocalisation and electron hopping occurs throughout the whole structure. A result of the structures symmetry as it is composed of equivalent addenda metal centres. The existence of belt and cap positions in Wells-Dawson clusters leads to delocalisation and 'hopping' occurring independently within each region. Distinct IVCT bands occur upon successive reductions, hence monitoring the IVCT band can be a powerful diagnostic tool to measure the progress of reduction of POM species.³⁵

1.5 Polyoxometalate Catalysis

POMs have extensively been used for catalysis, their inherent chemical and structural properties have been used in acid, base and photocatalysis. Precise control of the catalytic sites can be achieved by functionalisation with transition metals and inorganic ligands to tune redox, acid, and base properties.^{37, 38} These features combined with their oxidative and thermal stability mean POMs show considerable potential in catalysis. Base catalysis has been explored due to several benefits POMs have over commercial catalysts. These include quantifiable basic properties due to the basic sites typically being their surface oxygen atoms and their basicity being directly proportional to their size, anion charge and structure. These reactive oxygen atoms can remove protons and attack electrophiles which is useful in numerous base catalysed reactions.³⁹ POMs have also been used in acid catalysis reactions including Friedel-Crafts, condensation and amination reactions. Their use as strong acid catalysis arises from the Brønsted acidity of their protonated polyanions which further shows the flexibility of POMs in catalysis.⁴⁰

The fully oxidised transition metal framework of POMs denoted by empty d orbitals (d^0) gives rise to attractive redox properties, in particular multi electron reversible reductions, generating a potential for use as oxidation catalysts.⁴¹ This rich redox chemistry promotes photocatalytic applications facilitated by POMs innate UV absorptions. The UV absorption arises from the LMCT localised on the

terminal oxo-ligands and are core to POM photochemistry.⁴² The targeted photo-excitation of the O→M band promotes an electron from the doubly occupied bonding highest occupied molecular orbital (HOMO) to the antibonding lowest occupied molecular orbital (LUMO) (typically an O 2p→ M d orbital transition).³⁴ This transition produces a charge separated state with a localised d¹ metal centre and a radical on the oxo-ligand (Figure 10). The oxo radical can then abstract a proton from a substrate (S) and is the basis for POM photocatalysis. Furthermore, the d¹ centre becomes trapped, the resultant mixed valence POM is a heteropoly blue species (mentioned above) which displays strong visible light absorption in the form of IVCT bands.⁴³

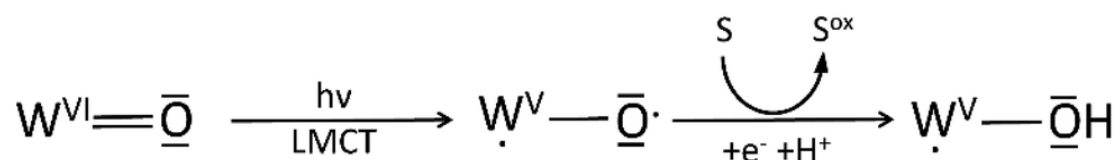


Figure 10: The photoreduction of a tungstate POM followed by substrate oxidation. Reproduced with permission from ref 43

Perhaps the biggest limitation of POM photocatalysis is their weak visible light absorption. Whilst the heteropoly blues do display strong vis absorptions, excitation of these bands does not result in significant photocatalytic activity.⁴² On top of this, reoxidation back to its base state to efficiently close the catalytic cycle can be challenging. Hence exploration into POM hybridisation has led to the development of novel photoactive hybrids as described above. Also, careful consideration into the choice of ligand and type of functionalisation method can allow for precise tailoring of the hybrids physical and chemical properties. Photocatalytic applications can be enhanced by the addition of a suitable chromophore, addition of a visible light active species can overcome the deficit in POMs visible light absorbance. The mechanism for photoexcitation is dependent on excitation of a chromophore ligand (L) followed by intermolecular charge transfer (Figure 11). The photoexcited state of L can transfer an electron to a POM metal centre forming a charge separated state, where a hole is left in the chromophore species and the POM centre has been reduced. The addition of a sacrificial

reductant can restore the ground state of the chromophore trapping the POM in its mixed valence state. This can be used in photocatalysis through oxidation of a substrate or exploiting the charge accumulation of the POM species.⁴³

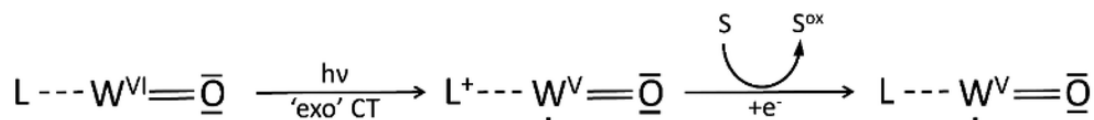


Figure 11 Photo excitation of chromophore ligand and subsequent intermolecular charge transfer and charge accumulation on a tungstate POM. Following this oxidation of a substrate. Reproduced with permission from ref 43.

1.6 Photoactive Hybrid Polyoxometalates

Within the literature a plethora of examples of hybrid POM photocatalyst exist, implementing both class I and class II hybridisation strategies.^{9, 42, 43} The seminal work of Fay et al. explored class I POMs for photocatalytic reactions, the group recognised the potential of the Wells-Dawson anion $[S_2M_{18}O_{62}]^{4-}$ as a photo induced oxidation catalyst. By combining the Wells-Dawson anions with $[Ru(bpy)_3]^{2+}$ cations they found conclusive evidence of visible light sensitisation of the POM and substantial visible light photoreduction of the POM species in the presence of benzyl alcohol.⁴¹ More recently perylene diimide (PDI) ligands have been used by Zhang et al. to form PDI-POM nanofibers. Not only were they able to form them via a simple solution dispersion method, but also observed fluorescence quenching and intermolecular charge transfer from the perylene to the POM. The PDI-POM nanofibers also enable increased photodegradation of methylene blue which was not observed in the PDI fibres alone. The group was able to show the importance of association of the perylene unit with the POM in creating long lived charge separated states which facilitate photodegradation.⁴⁴ Perylenes were also explored by Li et al. forming class I hybrids from $H_4[SiW_{12}O_{40}]$ and PDIs. Hybridisation of the POM and PDI ligand played a crucial role in the visible light photo-oxidation of 2-chloroethyl ethyl sulphides (Figure 12). The improved photochemical stability and enhanced

intermolecular charge transfer produced photocatalytic conversion of up to 99.9% compared to 57.1% of the PDI on its own.⁴⁵

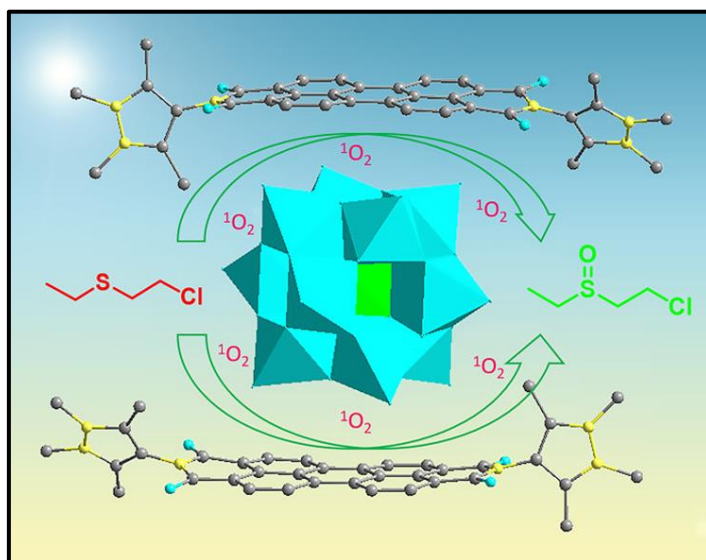


Figure 12: Schematic of the photo-oxidation of 2-chloroethyl ethyl sulphide using PDI-Keggin catalysts. Reproduced with permission from ref 45.⁴⁵

Despite the clear benefits of class I hybrids including proven visible light sensitisation, intermolecular charge transfer and ease of synthesis, significant research has gone into covalent functionalisation to form class II POM chromophore species. Primarily improved control over POM chromophore ratios and better stability to pH, temperature and solvent conditions has continued to drive interest in class II photocatalytic hybrids. Often class II hybrids are formed from Keggin or Wells-Dawson lacuna due to their impressive redox abilities and ease of functionalisation. An early example of covalent functionalisation of a Keggin POM was reported by Bonchio et al. the lacunary Keggin; $[\gamma\text{-SiW}_{10}\text{O}_{36}]^{8-}$ was hybridised with C₆₀-fulleropyrrolidines (Figure 13). The new catalytic system was found to produce high catalytic turn over (ca. 90%) for the photooxidation of phenols and organic sulphides. Furthermore, analogous materials were tested, those lacking the fullerene group showed no photocatalytic activity and changing stability trends were observed with adaption to the linker chain length, stressing the importance of molecular design.^{34, 46}

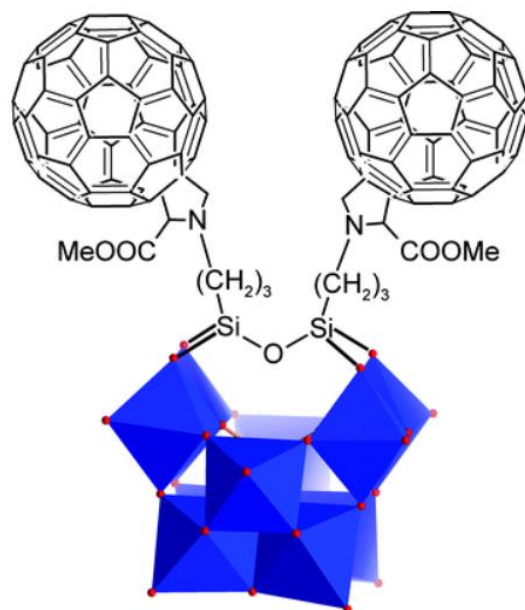


Figure 13: Illustration of class II hybrid; $[\gamma\text{-SiW}_{10}\text{O}_{36}]^{8-}$ covalently functionalised with C_{60} -fulleropyrrolidines used as a photocatalyst for phenol and organic sulphide photooxidation. Reproduce with permission from ref 34³⁴

One of the few examples of a PDI being covalently grafted to a POM is the work of Harriman et al. as with the work of Zhang and Li intermolecular charge transfer and fluorescence quenching was observed from the PDI ligand to the POM. They found that the PDI sensitiser can undergo two successive reductions, the electrons are then transferred and stored on the POM core. As with the groups previous work they found that a more flexible linker was key to improving intermolecular charge transfer.⁴⁷

From the literature we have seen a significant advancement in hybridisation strategies between chromophore and POM species. Improved photocatalytic efficiency has been shown for numerous reactions and is convincing for the benefit of POM-chromophore hybrids. PDI-POM hybrids have shown favourable charge transfer mechanics and warrant further investigation.

1.7 Perylene Diimides

1.7.1 Introduction to Perylene Diimides

Perylene-3,4,9,10-Tetracarboxylic Diimides (PDI) have extensively been used in industrial processes dating back to the early 1910s, when its parent compound perylene-3,4,9,10-tetracarboxylic dianhydride (PTCDA) was first discovered.⁴⁸ It was found that subtle changes to the chemical structures of PDIs produced a variety of pigments from red to black shades.⁴⁹ In addition, the chemical, thermal and photo stability of PDIs made them ideal for high grade industrial paints where their durability outweighs their high cost.⁵⁰ At present PDIs have been integrated in modern electronics, their high fluorescence quantum yields and extinction coefficients are ideal for: organic light emitting diodes (OLEDs),⁵¹ solar cells and organic field effect transistors (OFETs)⁵² to name a few. Despite their ideal chemical and electronic properties, perylene derivatives have been limited by their tendency to form aggregates. Aggregation results from π - π stacking interactions caused by their extended planar aromatic structure, decreasing solubility and quenching fluorescence.^{52, 53} The prevalence of PDIs in modern electronics has generated significant interest in tuning the optical properties of PDIs whilst also considering the limitations arising from their poor solubility.

The robust nature of PDIs combined with the diverse range of modifications that can be applied to tune their chemical and optical properties make them an ideal choice of chromophore for POM hybridisation. As described above, a precedent has already been set for producing POM hybrids with perylene derivatives. The work of the Zhang, Li and Harriman groups have already displayed promising intermolecular charge transfer and catalytic properties of perylene POM hybrids. Clearly perylene ligands show promise for improving electronic and photochemical properties of POMs, however their covalent hybridisation with POMs needs to be explored further.

1.7.2 Perylene Diimide Structure

The aromatic core of PDIs consists of two naphthalene units joined by two bonds forming a fused five-ring conjugated system. The core is divided into three subsections, Figure 14 defines the numbering system and highlights these key positions. Two regions exist within the aromatic core: first the bay region, which encompasses the central positions of the aromatic core (1, 6, 7 and 12) and the ortho region, consisting of the positions adjacent to the carbonyls (2, 3, 4, 5, 8, 9, 11 and 10). The third region often referred to as the imide position is comprised of the two terminal imide groups connected to the aromatic core.

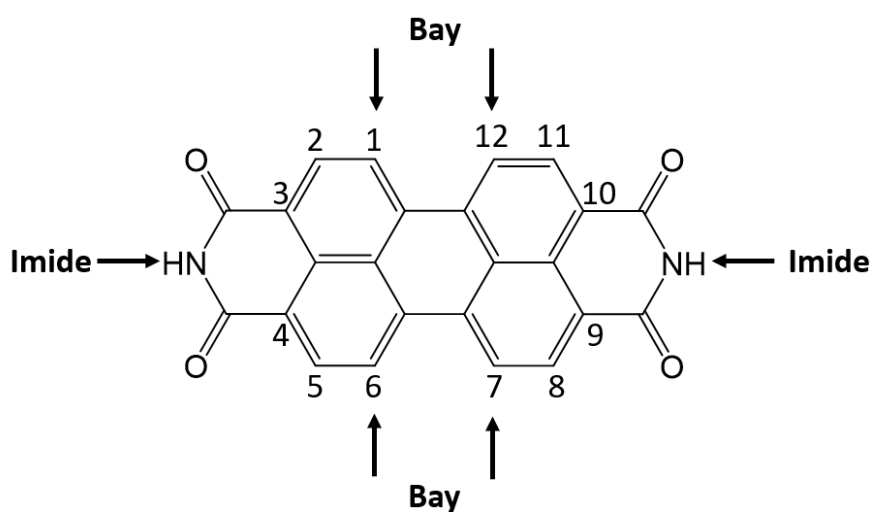


Figure 14: Diagram showing the structure and key positions of perylene diimide.

1.8 Optical and Electronic Properties of Perylene Diimides

The optical properties of PDIs are of particular interest, a broad $S_0 \rightarrow S_1$ absorption band leads to a vibrational structure with absorption maxima typically in the range of 500-600 nm and large extinction coefficients of 10^5 order of magnitude.⁵⁴ Three key transitions occur in the vibronic structure of PDIs, the $0 \rightarrow 0$, $0 \rightarrow 1$ and $0 \rightarrow 2$ transitions. This results in three distinct absorption peaks typically centred around 525 nm, 495, nm and 460 nm.^{55, 56} Density functional theory (DFT) calculations on PDIs reveal the nature of their frontier orbitals. The frontier orbitals are almost entirely localised on the perylene

core (Figure 15), DFT calculations also indicate the $S_0 \rightarrow S_1$ transition is a HOMO \rightarrow LUMO excitation.⁵⁰ The largest orbital coefficients for both the HOMO and LUMO are found in the bay and ortho positions. Hence, the $S_0 \rightarrow S_1$ transition can be considered entirely localised on the core of the PDI and the absorption and emission properties of PDIs are primarily controlled by modification of the perylene core.⁵⁷ As expected, attaching groups to the perylene core has been found to cause a shift in the $S_0 \rightarrow S_1$ absorption band, allowing for fine tuning of electronic properties by careful selection of functional groups.^{55, 58} Importantly both of PDIs frontier orbitals exhibit a node that coincides with the imide positions. Hence modification to the imide position has little to no effect on the $S_0 \rightarrow S_1$ transition, a result of limited electronic interaction between the core and imide substituents.⁵⁴

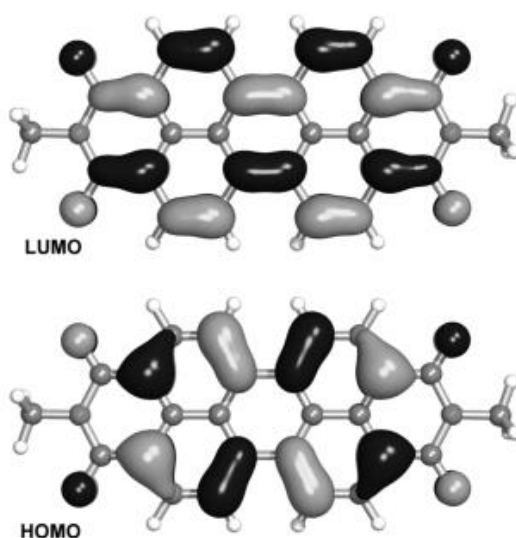


Figure 15: Frontier orbitals of *N,N*-dimethyl PDI, calculated by DFT. Reproduced with permission from ref 50.⁵⁰

Cyclic voltammetry (CV) data has been used to further probe the electronic character of PDIs, generally two one electron reversible reductions and a reversible oxidation can be expected. The first and second reduction potentials are found in the region of -0.6 and -1.5 V, suggesting a fairly electron deficient core.^{50, 59} The reduction potentials can be fine-tuned by introducing electron withdrawing groups to the core, increasing electron deficiency and positively shifting reduction potentials. Conversely, electron donating groups can be used to decrease electron deficiency and negatively shift

reduction potentials.^{60, 61} The high photochemical stability of PDIs arises from their electron deficient character, photooxidation is the major degradation mechanism of chromophores and is unfavourable. Precise tuning of the molecule's electronic structure whilst remaining chemically stable are the key properties that make PDIs particularly attractive as chromophores.

1.9 Modification of Perylene Diimides

The unique electronic structure of PDIs allows for the core to be considered electronically decoupled from the imide substituents which generates two distinct areas of modification on the PDI. The first group of derivatives are obtained from bonding groups to the nitrogen atom located on either imide position. The nodes present in the imide position allow modifications to be made here, examples include the addition of solubilising groups or adding new functionalities without effecting its absorbance and emission properties. This was first described by Langhals et al where it was found groups added to the imide position can significantly increase solubility of PDIs in organic solvents.⁵³ It was reported that even simple branched alkanes can greatly solubilise the PDI by disrupting the π - π stacking interactions.

Perhaps the most explored category of modifications, functionalisation of the bay position can be used to optimise the optical, electronic, and redox chemistry of PDIs. Bay substitution has become the predominant method of tuning perylene optical and electronic properties. Addition of groups to this position can result in a combination of large bathochromic shifts in the absorption maxima and shifts in the materials reduction potentials.^{62, 63} Substitution at the bay position first requires bromination of the perylene core. This reaction results in a mixture of products and can be difficult to separate. Separation often has to occur after the subsequent imidization step, which can cause bay substitution to have poor yields.⁶⁴ Whilst substitution in the bay region is primarily used to tune its optical and electronic properties, they also solubilise the PDI. Chai et al demonstrated through DFT calculations that introducing groups to the bay position not only allows manipulation of the electronic properties but can also introduce a twist to the perylene core at angles as large as 35 °. This significant distortion

to the PDI backbone disrupts π - π stacking interactions, solubilising the material and can even facilitate improved electron transport properties.^{65, 66}

2. Aims

This project aims to develop a photoactive POM hybrid for photochemical applications. A novel phosphorylated PDI will be developed for the purpose of hybridising with a POM. The PDI chromophore should impart visible light sensitisation to the POM hybrid, furthermore, the chromophore should display synergistic electron transfer to the POM core to develop a new photocatalytic dyad. For the purpose of photocatalytic reactions, the hybrid should produce long lived charged separated states under visible light irradiation. Perylene diimides have been explored as the chromophore due to their robust chemical, thermal and photostability as well as their intense visible light absorptions. Wells-Dawson polyoxotungstates were selected as the POM structure for hybridisation. This selection was made to take advantage of the unique redox properties and stability of Wells-Dawson POMs, the tungstate species form the most stable and reactive lacunary structures allowing for simple modification with phosphorylated PDI dyes.

Hybridisation approaches will be explored to develop an efficient method of synthesising the target material. A combination of analytical techniques will be employed to fully characterise the hybrids' structure, including nuclear magnetic resonance (NMR) spectroscopy, mass spectrometry (MS) and thermogravimetric analysis (TGA). In addition, electrochemical and photochemical characterisation of the hybrid will be carried out to assist in evaluating the redox and photocatalytic performance of the new material. Finally, comparisons will be made to the precursor units to confirm hybridisation and to observe any synergistic functionality between the PDI and Wells-Dawson POM.

3. Results and Discussion

The process of producing a visual light sensitised perylene-POM hybrid requires several synthetic steps. The synthetic process has been divided into two stages, first synthesis and characterisation of the POM species followed by design and synthesis of a suitable PDI chromophore.

3.1 Synthesis and Characterisation of Polyoxometalate Precursors

As specified earlier, Wells-Dawson polyoxotungstates (POTs) produce the most stable lacunary structures, hence they were selected as the ideal target for POM hybridisation.⁶⁷ The goal of producing a suitable photocatalytic material begins with synthesising the Wells-Dawson POT, $K_6[P_2W_{18}O_{62}]$ (**P₂W₁₈**) and its subsequent lacunary structure $K_{10}[P_2W_{17}O_{61}]$ (**P₂W₁₇**).

The key synthetic steps to form **P₂W₁₈** were undertaken following the method described by Graham and Finke with an adapted work up.⁶⁸ The 'one-pot' synthesis of **P₂W₁₈** begins with an acid mediated self-assembly reaction of tetrahedral $[WO_4]^{2-}$ metal-oxide fragments obtained from Na_2WO_4 dissolved in water. Reduction in pH through the dropwise addition of 4 M HCl causes the $[WO_4]^{2-}$ fragments to protonate and expand their coordination sphere to form larger octahedral units. These units then assemble into bimetallic and trimetallic structural groups, refluxing for 24 h ensures complete conversion. Crucial for directing the self-assembly mechanism is the addition of PO_4^{3-} ions obtained through dropwise addition of H_3PO_4 , the polyhedra assemblies condense around the templating anion to form the larger Wells-Dawson structure. A white precipitate that forms during the addition of HCl identified as $K_{10}[P_2W_{17}O_{61}]$ impurities can be prevented by using an excess of H_3PO_4 . Graham and Finke expanded upon this; they found that the additional H_3PO_4 completes the acidification of the $K_{10}[P_2W_{17}O_{61}] / [WO_4]^{2-}$ solution forming $[\alpha-P_2W_{18}O_{62}]^{6-}$. Precipitation of the POM is facilitated by the addition of KCl to produce $K_6[P_2W_{18}O_{62}]$. It is common for the POM to be reduced during the synthesis distinguished by the green colouring of the crystals. Liquid bromine can be used to re-oxidise the crystals with a distinct colour change to yellow. The method proposed by Graham and Finke suggests a slow solution evaporation over one week produces the highest purity crystals of $K_6[P_2W_{18}O_{62}]$.

However, we found a simple recrystallisation from boiling water produced the crystals in acceptable yield and purity.

The method described by Constant et al for the formation of the mono lacunary Wells-Dawson, P_2W_{17} was used.²⁰ Due to the instability of P_2W_{18} in base, one W=O unit can be hydrolysed leaving the α_2 -monolacunary form of the Wells-Dawson POM. This was done by exposing the plenary P_2W_{18} structure to alkaline conditions using a 1 M solution of $KHCO_3$. After 1 h complete conversion of P_2W_{18} to P_2W_{17} denoted by the formation of a white precipitate was observed. Once again, a simple recrystallisation from boiling water produced P_2W_{17} crystals in high yield and purity.

The primary method of characterising the Wells-Dawson POMs is by using ^{31}P NMR spectroscopy to investigate the environment of the PO_4 templating ions. Phosphorus atoms were chosen for NMR spectroscopy over analysing other atoms within the POM. This is because it is cheaper and more sensitive than ^{17}O and ^{183}W NMR spectroscopy which requires higher temperatures and several days to produce good spectra. P_2W_{18} contains two phosphorus anions in equivalent environments. It is predicated that a single peak in the ^{31}P NMR spectrum will be observed. In contrast the loss of a W=O unit removes the symmetry of the environments hence two phosphorus peaks should be seen in the NMR spectrum of P_2W_{17} . Figure 16 shows the results of NMR spectroscopy, as predicted a single peak is observed at $\delta = -13.01$ ppm for P_2W_{18} whereas P_2W_{17} shows two peaks at $\delta = -7.26$ ppm and $\delta = -14.34$ ppm. The peak at $\delta = -7.26$ ppm can be assigned to the phosphorus anion at the open end of the POM due to less shielding after the removal of a W=O unit.

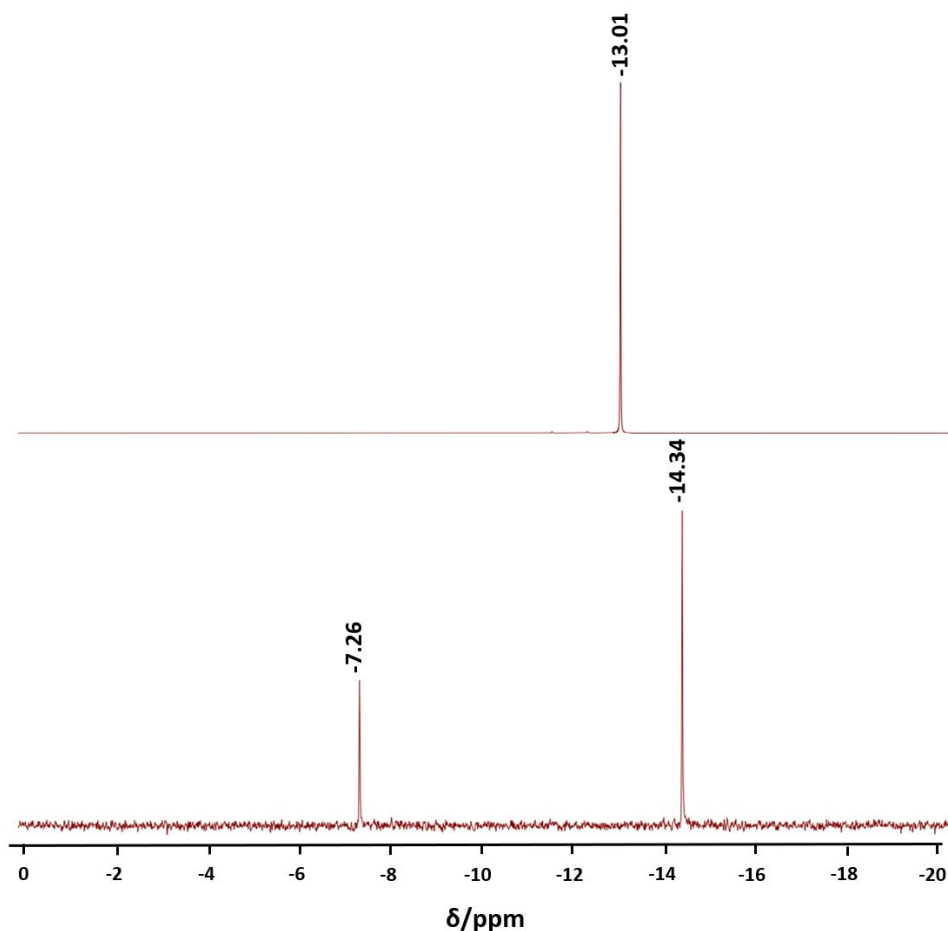


Figure 16: ^{31}P NMR spectrum in D_2O for P_2W_{18} (top) and P_2W_{17} (bottom). Key peaks have been labelled.

To supplement the findings of NMR spectroscopy, electrospray ionisation mass spectrometry (ESI MS) was used. ESI-MS is ideal for larger molecules and can produce several fragments that can be assigned to confirm the structure. Several anions of P_2W_{18} were located supporting its synthesis (Table 1 and Figure 17).

Table 1 Selected ESI-MS assignments for P_2W_{18} .

Assignment	Z	m/z (calc)	m/z (obs)
$\{\text{H}_3[\text{P}_2\text{W}_{18}\text{O}_{61}]\}^{3-}$	3-	1457.59	1457.54
$\{\text{KH}_2[\text{P}_2\text{W}_{18}\text{O}_{61}]\}^{3-}$	3-	1468.41	1468.53
$\{\text{Na}_4[\text{P}_2\text{W}_{18}\text{O}_{61}]\}^{2-}$	2-	2222.74	2222.73
$\{\text{Na}_3\text{H}[\text{P}_2\text{W}_{18}\text{O}_{61}]\}^{2-}$	2-	2219.23	2219.8

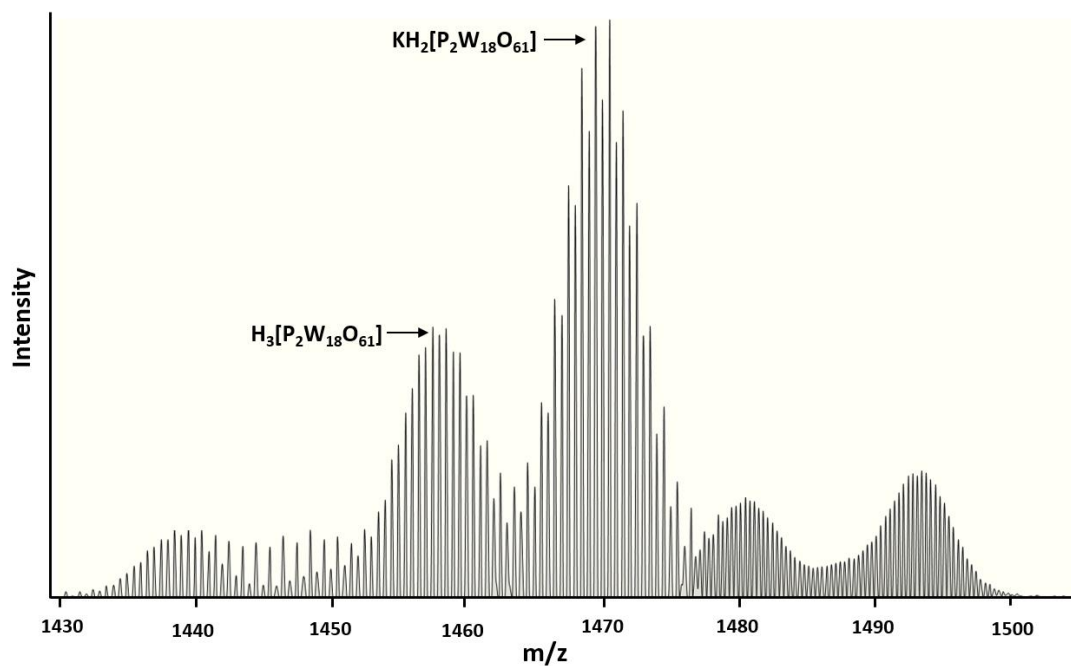


Figure 17: A section of the ESI mass spectrum for P_2W_{18} in the range of 1430-1500 m/z . Some fragments have been annotated

ESI-MS was also used to analyse the Lacuanry P_2W_{17} . Once again, several anions were located confirming the synthesis of P_2W_{17} (Table 2 and Figure 18).

Table 2 Selected ESI-MS assignments for P_2W_{17}

Assignment	z	m/z (calc)	m/z (obs)
$\{Na_4[P_2W_{17}O_{61}]\}^{2-}$	2-	2127.38	2127.15
$\{Na_3K[P_2W_{17}O_{61}]\}^{2-}$	2-	2139.10	2139.13
$\{Na_2K_2[P_2W_{17}O_{61}]\}^{2-}$	2-	2145.10	2145.11
$\{K_4[P_2W_{17}O_{61}]\}^{2-}$	2-	2161.07	2161.10

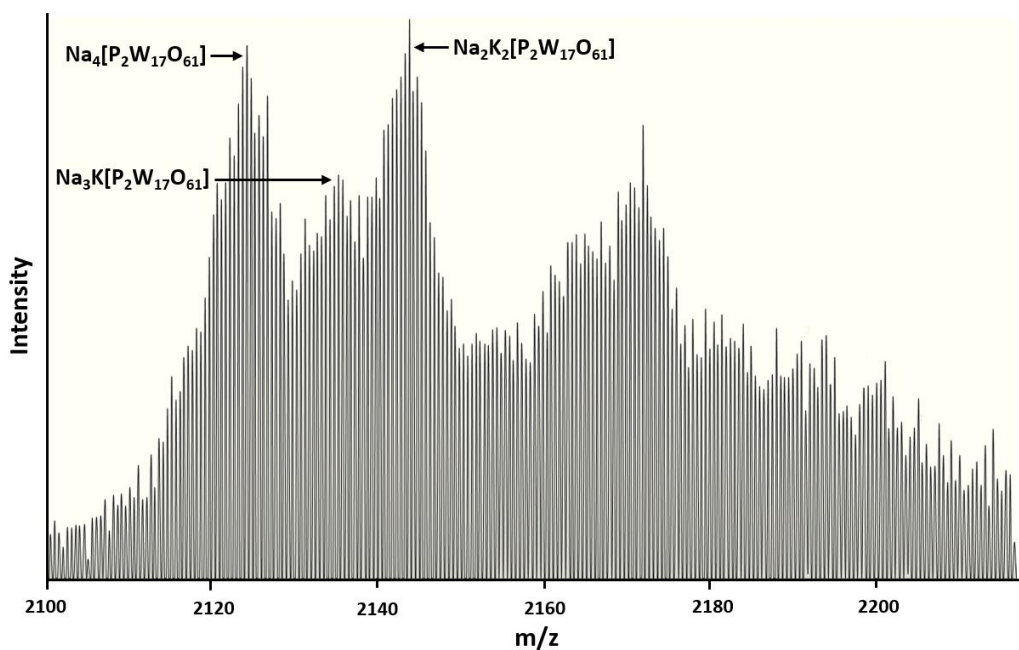


Figure 18: A section of the ESI mass spectrum for P_2W_{18} in the range of 2100-2200 m/z . Key fragments have been annotated.

3.2 Synthesis and Characterisation of Asymmetric PDI Precursor

When designing PDIs for more intricate molecular systems it may be desired to create a PDI with divergent groups on each imide position. For the purpose of hybridising a perylene with a POM an anchorage group is needed, however, it may also be desired that a group be added to improve the solubility of the PDI hence the choice to design and synthesise an asymmetric PDI was made.

3.2.1 Synthesis of PTE and PDE

One of the most versatile and reliable methods for synthesising asymmetric PDIs was first described by Xue et al.⁶⁹ The process begins by forming the perylene-3,4-anhydride-9,10-dicarbonyl (**PDE**) intermediate followed by the sequential addition of terminal groups through amine condensation with the anhydride positions. Figure 19 describes the overall synthetic steps required to produce an asymmetric PDI. First formation of perylene-3,4,9,10-Tetraester (**PTE**) is achieved by esterification of PTCDA with a long chain halogenated alkane. In this instance decyl bromide was used; the flexible

decyl units act as a solubilizing group, providing sufficient organic solubility for subsequent perylene derivatives.

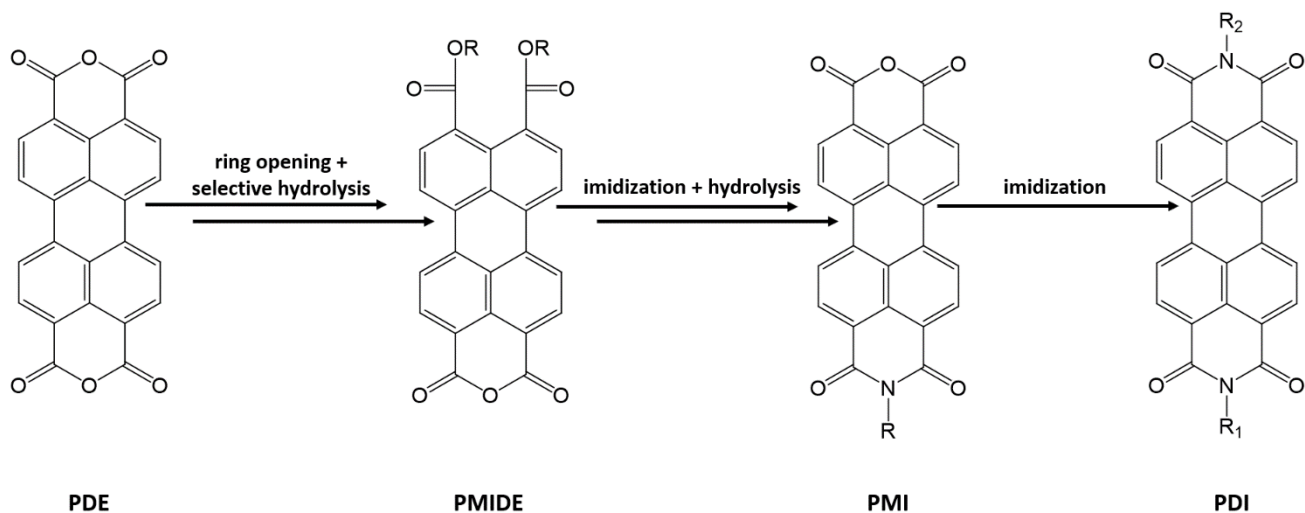


Figure 19: Schematic summary showing the overall synthetic steps to produce an asymmetric PDI from PTCDA

The second and most crucial step in the synthesis is the 'selective' hydrolysis of **PTE** to **PDE**, it is envisioned that by exploiting the solubility difference between the two molecules the product can be removed from solution before the second ring closure can occur. The optimised conditions suggested by Xue et al. established that a solvent mixture of dodecane and toluene (5:1 v/v) sufficiently solubilised **PTE** however, **PDE** would be insoluble. The strong organic acid p-Toluenesulfonic acid monohydrate (PTSA.H₂O) was added to the reaction. PTSA.H₂O serves as both the acid catalyst and water source for the hydrolysis, conveniently PTSA.H₂O is a solid hence it will not alter the solvent ratio. Figure 20 illustrates the dynamic equilibrium where the target molecule can only form when acid catalysed hydrolysis occurs to adjacent esters. Acid hydrolysis being a reversible process allows the reaction to correct itself if the 'wrong' esters are hydrolysed, with the equilibrium being further driven forwards by the product precipitating out of solution.

the carbonyls at the imide position. This causes the phenyl ring to sit perpendicular to the plane of the PDI core disrupting π - π Interactions. It was hypothesised that stopper B would produce the greatest solubilising effect. This is because of a large steric clash between the ortho diphenyl groups and perylene carbonyls which prevents π - π Interactions.

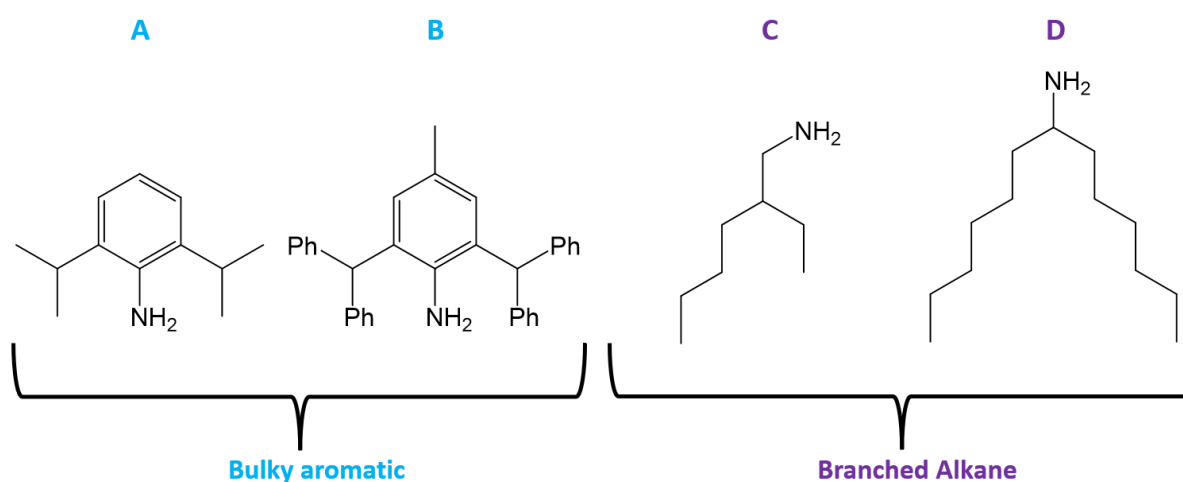


Figure 21: A selection of stopper groups used to solubilise PDIs. 'Bulky aromatics' (left) and branched 'swallow tail' alkanes (right)

Initial attempts to synthesise **PMIDE** using stopper B proved unsuccessful likely owing to the large steric bulk of the group resulting in poor reaction yields. Reaction temperature was increased to facilitate overcoming the steric hinderance and improve reaction yields. However, unforeseen side products were introduced. It is hypothesised that the higher temperature and basicity of stopper B can facilitate ring closing followed by imidization. Subsequently, stopper group C was used to produce **PMIDE**, the use of a less sterically hindered stopper was envisioned to improve the reaction yield and allow reactions to be run at lower temperatures. Upon switching to stopper C, **PMIDE** was produced in yields of over 65% with no side products, a significant improvement over stopper B (Figure 22).

After producing the mono imide in high yields and purity the following step is the transformation of the remaining ester groups to an anhydride ring. As seen with the conversion of **PTE** to **PDE**, addition

of strong organic acid in the form of PTSA.H₂O facilitates the ring closing reaction. As expected perylene-3,4-imide-9,10-anhydride (**PMI**) was produced in high yields of over 90% (Figure 22).

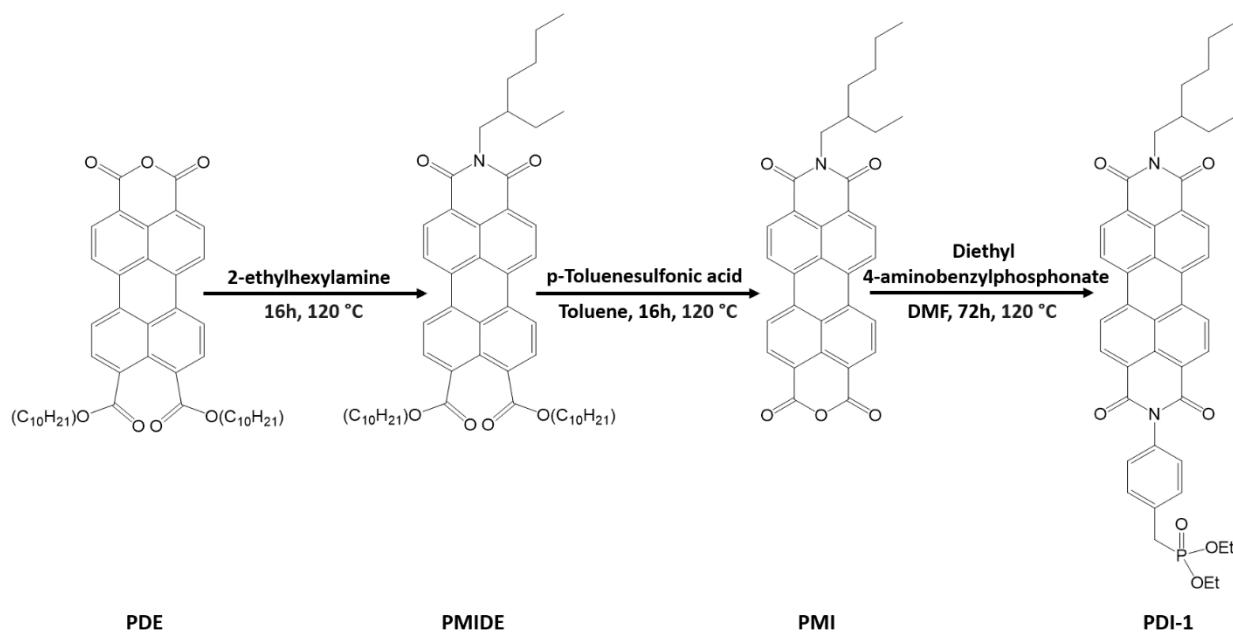


Figure 22: A summary of the overall synthetic steps undertaken to transform PDE to PDI-1

3.2.3 Synthesis and Characterisation of PDI

Once **PMI** was obtained, a second group could be added through a final condensation reaction. The lacunary precursor **P₂W₁₇** has four exposed terminal oxygens with increased nucleophilicity, these act as ideal sites for organo-functionalisation with appropriate electrophiles. Whilst organosilicates represent one of the most explored electrophiles used for functionalization, organophosphates are rapidly being explored as alternatives. It has been reported that organophosphorus linkers have caused significant shifts in ¹⁸³W and infrared spectroscopies as well as fluorescence quenching observed in naphthyl ligands, heavily suggesting intermolecular charge transfer.³² These results point to phosphorus linkers improving electronic conjugation between the POM and ligand.²⁷ Studies

undertaken by Harriman et al. into the effect on conjugation based on the group directly adjacent to the phosphorus linker, found improved conjugation with the addition of an aryl group between the phosphorus and the ligand.^{32, 47} Taking this into account, it was decided to use the aryl phosphonate linker diethyl 4-aminobenzylphosphonate, with the aim to improve conjugation between the two moieties. For the conversion of **PDE** to **PMIDE**, it was convenient that the ligand could also be used as the solvent however for conversion of **PMI** to **PDI-1** this was not an option. Whilst molten imidazole is a common choice for imidization solvents it was found that dry N, N-dimethylformamide (DMF) was more effective in solubilising **PMI**. Several attempts to optimise reaction time and temperature established that running the reaction for 72 h at 120 °C significantly improved reaction yield. This is significantly longer in contrast to the 16 h at 120 °C required for the first imidization. The longer reaction time is attributed to the increased steric bulk of diethyl 4-aminobenzylphosphonate, opposed to the smaller 2-ethylhexylamine molecules.

The ligand was characterised using complimentary NMR spectroscopy techniques, the ¹H NMR spectrum displayed the expected peaks in good integration (Figure 23).

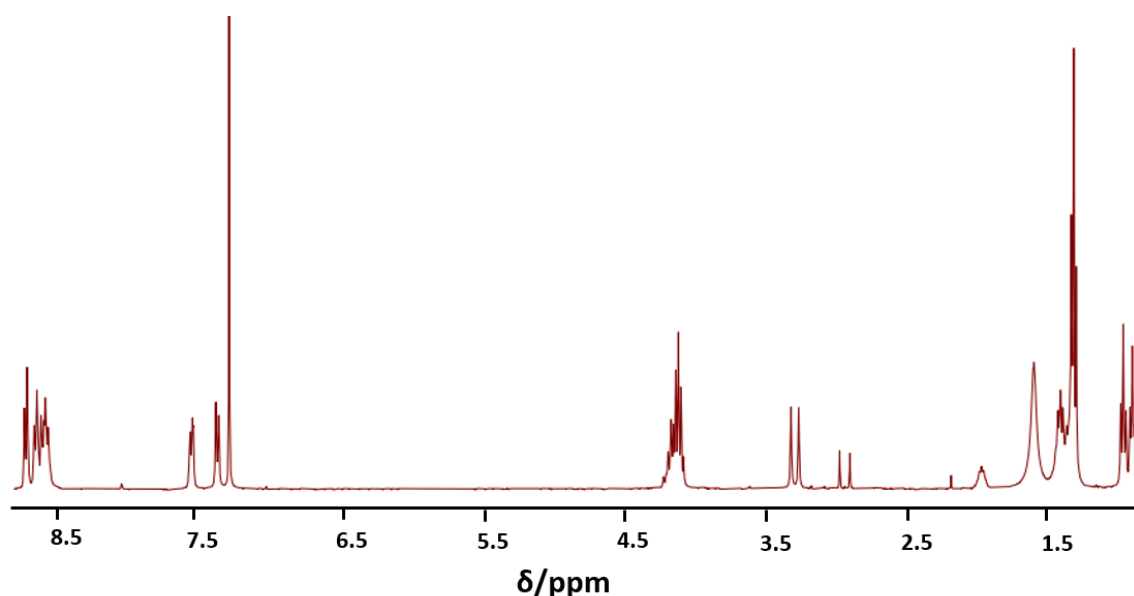


Figure 23: ¹H NMR spectrum in CDCl₃ of PDI-1. List of peaks with their splitting and J coupling (Hz): δ 8.66 (d, J = 7.9 Hz, 2H), 8.56 (d, J = 7.9 Hz, 2H), 8.50 (d, J = 8.1 Hz, 2H), 8.45 (d, J = 8.1 Hz, 2H), 7.56 – 7.49 (m, 2H), 7.36 (d, J = 7.8 Hz, 2H), 4.10 (dq, J = 14.7, 7.5 Hz, 4H), 3.32 – 3.23 (m, 2H), 1.99 – 1.88 (m, 1H), 1.62 (s, 2H), 1.44 – 1.17 (m, 12H), 0.95 (t, J = 7.3 Hz, 3H), 0.92 – 0.84 (m, 3H). Note residual DMF peak at 2.93 ppm

Notably the aromatic peaks for the phosphonate group have shifted from 7.08 and 6.64 ppm to 7.55 and 7.34 ppm, additionally the protons on the carbon adjacent to the phosphorus group have transformed from 3.05 ppm to 3.30 ppm providing further evidence of successful synthesis (Figure 24).

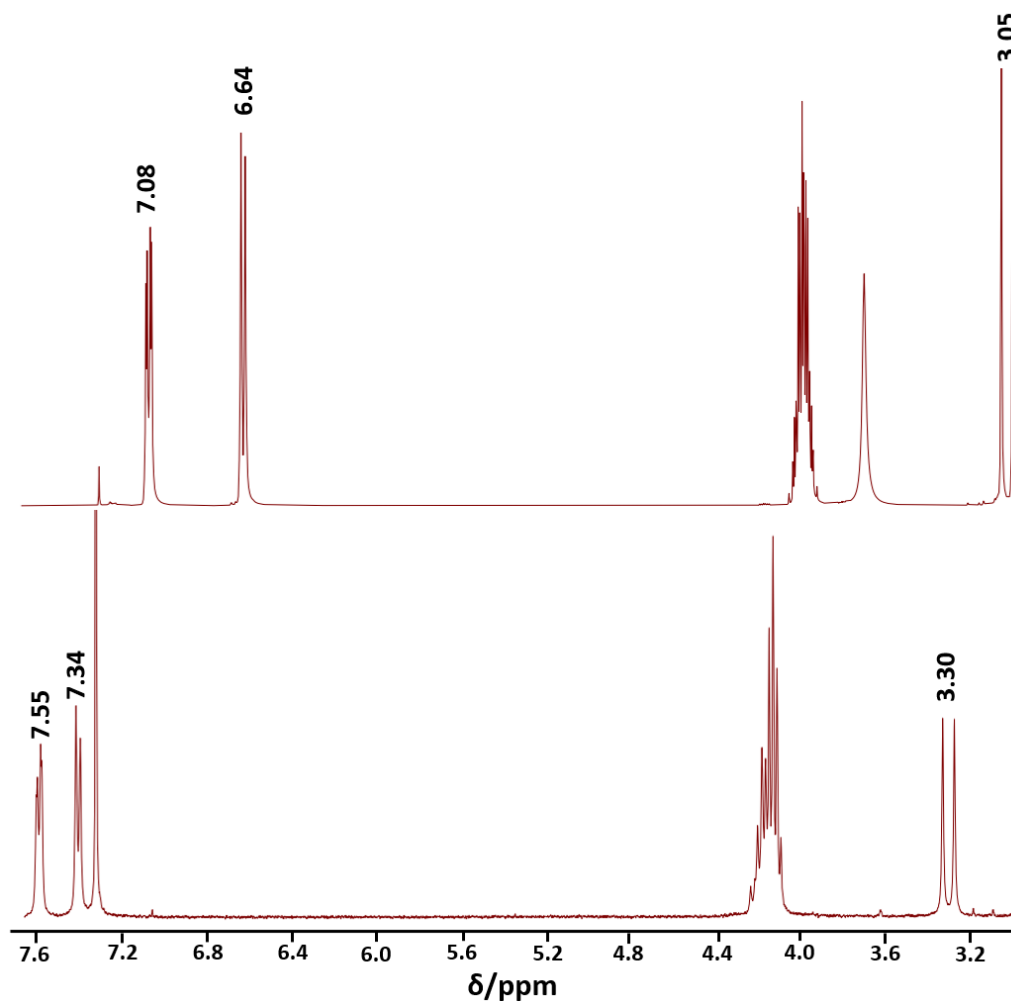


Figure 24: A section of the ¹H NMR spectrum in CDCl₃ in the range of 3-7.6 ppm for 4-aminobenzylphosphonate (top) and PDI-1 (bottom), Key peaks have been labelled.

³¹P NMR spectroscopy was a powerful tool to confirm synthesis and purity of **PDI-1**. A single peak at $\delta = 25.85$ ppm suggests the product is pure by ³¹P NMR spectroscopy further supported by a significant

shift compared to the phosphorus value for diethyl 4-aminobenzylphosphonate ($\delta = 27.17$ ppm) supporting results seen in the ^1H NMR spectrum (Figure 25).

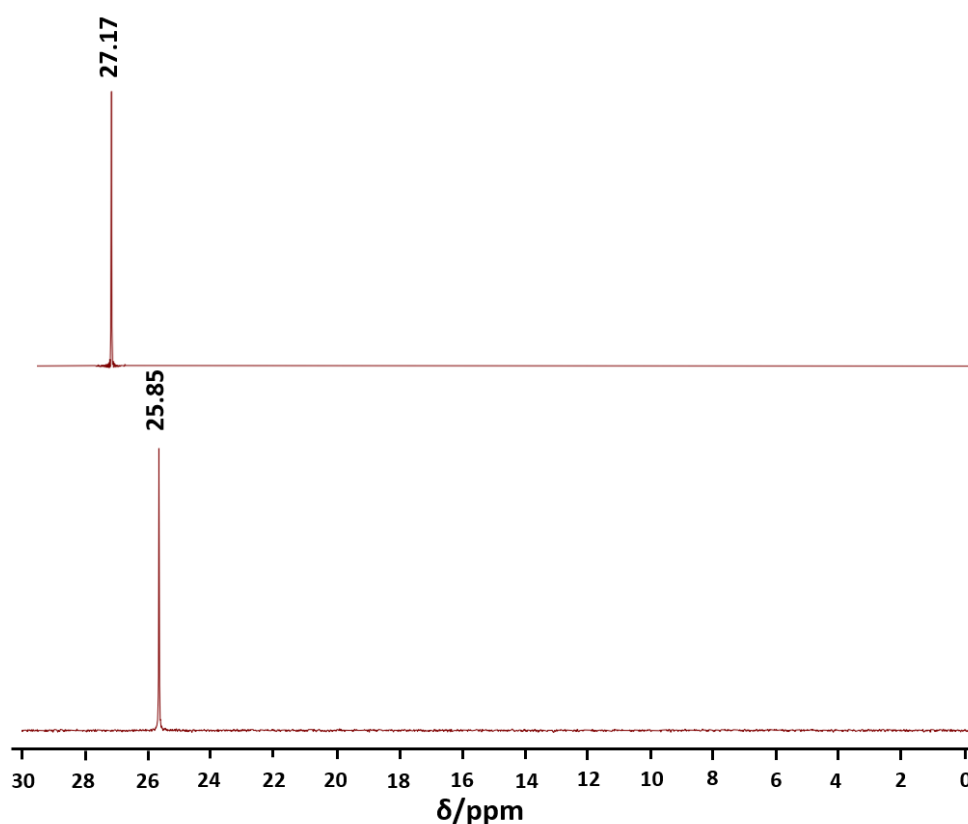


Figure 25: A section of the ^{31}P NMR spectra in CDCl_3 in the range of 0-30 ppm for 4-aminobenzylphosphonate (top) and PDI-1 (bottom), Key peaks have been labelled.

Matrix assisted laser desorption/ionisation (MALDI) mass spectrometry run in positive mode was used to give additional evidence to characterise **PDI-1**. MALDI-MS was used over ESI-MS for all perylene derivatives for two reasons; perylenes have limited solubility in ESI-MS solvents (MeCN, MeOH, H_2O) which meant ESI could not be used for all perylene compounds in addition MALDI produces singly charged species improving ease of spectral analysis.⁷⁰ The singly charged cation $\{\text{C}_{43}\text{H}_{41}\text{N}_2\text{O}_7\text{P}\}^+$ was identified at an observed mass of 729.09 m/z. This further supports the synthesis of **PDI-1** as suggested by the NMR spectroscopy findings.

Deprotection of the PDI product was undertaken following the McKenna method (Figure 26).^{71, 72} Facile dealkylation of **PDI-1** is achieved by addition of 10 equivalents of bromotrimethylsilane in dry dichloromethane at room temperature, after one day the corresponding silyl ester was produced. Addition of protic solvents such as methanol allows for rapid hydrolysis of the ester groups producing **PDI-2** in quantitative yields.

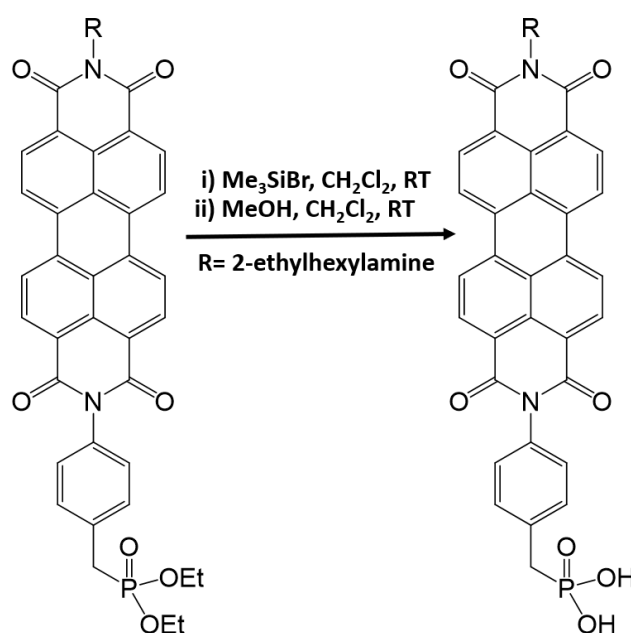


Figure 26: Scheme showing the deprotection of **PDI-1** to **PDI-2** via the McKenna method.

Despite the addition of the branched alkyl chain as a solubilising group, conversion of the protecting esters to di-hydroxyl functionality caused a significant reduction in organic solubility. This led to difficulties in characterisation in particular poor solubility in common NMR spectroscopy solvents. Addition of < 1% triethylamine (TEA) to D_2O increases the pH enabling deprotonation of the OH groups and solubilising **PDI-2**. The compound was deemed pure by ^{31}P NMR spectroscopy (Figure 27), a single peak at $\delta = 16.81$ ppm was observed. The significant solubility change combined with the fact that **PDI-1** is not solubilised in the TEA/ D_2O solvent further supports the formation of **PDI-2**.

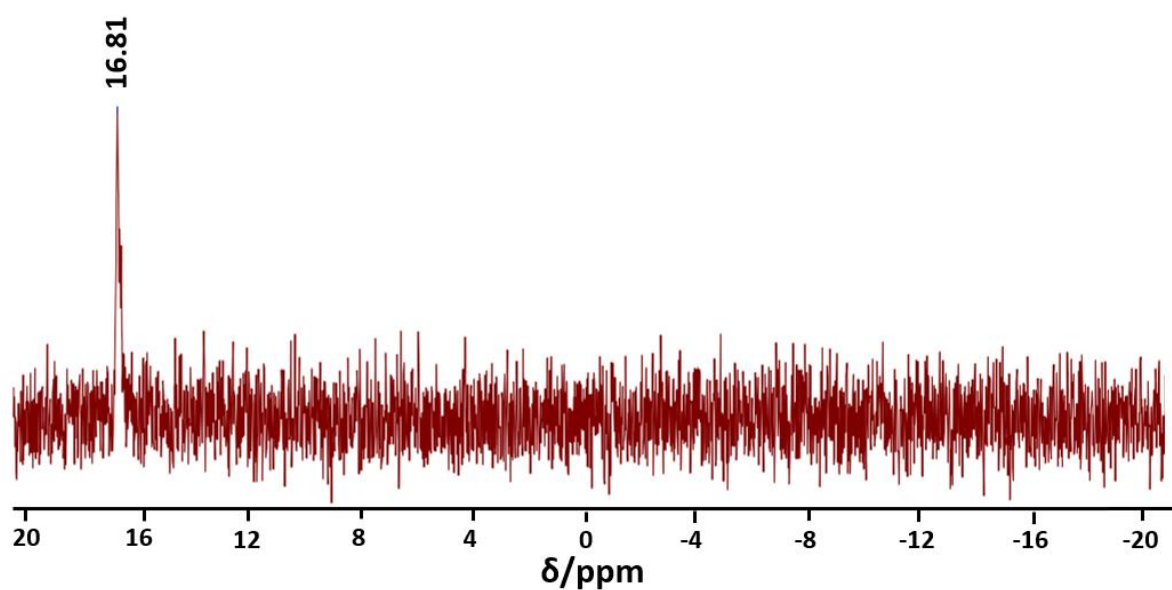


Figure 27: ³¹P NMR spectrum of PDI-2 in D₂O/TEA (99:1), δ =16.81 ppm

MALDI MS was also run on **PDI-2** to further confirm dealkylation. Table 3 gives the key assignments.

The ions of **PDI-2** were located via MS confirming the success of the deprotection step.

Table 3: Selected MALDI-MS assignments for PDI-2

Assignment	Z	m/z (calc)	m/z (obs)
{[C ₃₉ H ₃₃ N ₂ O ₇ P]} ⁺	1+	672.66	673.24
{[C ₃₉ H ₃₃ N ₂ O ₇ P+Na]} ⁺	1+	695.65	695.21
{[C ₃₉ H ₃₃ N ₂ O ₇ P+K]} ⁺	1+	711.76	711.19

3.3 Synthesis and Characterisation of Polyoxometalate Hybrid

Hybridisation of a wells-Dawson polyoxometalates has been reported numerous times in the literature, hybrids were produced following an adapted general procedure outlined by Fujimoto et al.^{5, 9, 22, 73} Hybridisation occurs via a condensation reaction of the reactive lacunary P_2W_{17} and **PDI-2**, 12 equivalents of 12 M HCl were added to the reaction mixture to facilitate condensation. The reaction was initially attempted in DMF at 85 °C for 24 h, analysis of ^{31}P NMR spectroscopy data (Figure 28) displayed a single peak at $\delta = -13.24$. This peak is concurrent with the peak for P_2W_{18} (in MeCN- d_3) suggesting conversion of the metastable lacunary P_2W_{17} back to its plenary form.

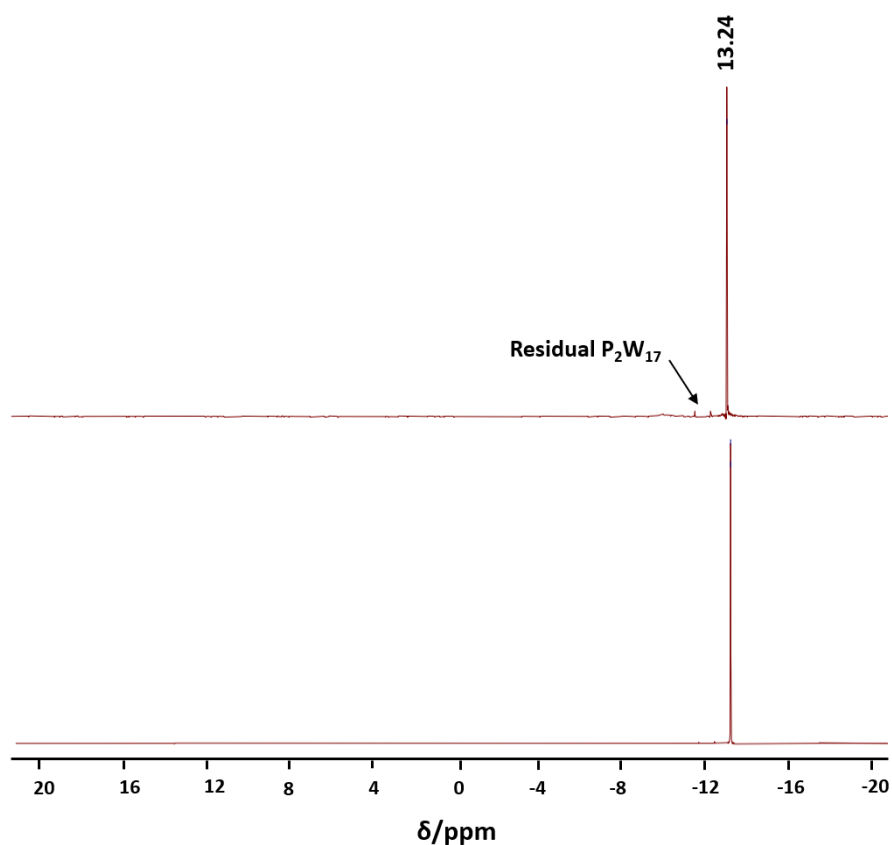


Figure 28: ^{31}P NMR spectra in MeCN- d_3 for the failed synthesis of PDI-POM hybrid (top) and P_2W_{18} (bottom). Key peaks have been labelled including residual P_2W_{17} .

It was hypothesised that the poor solubility of **PDI-2** in DMF limited rate of reaction and favoured rearrangement P_2W_{17} to P_2W_{18} . To improve ligand solubility the higher boiling solvent N, N-

dimethylacetamide (DMA) was selected. This solvent displayed better solubility for **PDI-2**, complete dissolution of the ligand was confirmed before adding additional reagents to favour the reaction of the **P₂W₁₇** with **PDI-2**. Upon work up of the reaction a dark a red solid was obtained, the first evidence of formation of a new material was its solubility in acetonitrile (a solvent that both precursor materials are poorly soluble in). Initial ¹H experiments in CD₃CN produced broad peaks with poor resolution making assigning the spectra challenging, changing the NMR spectroscopy solvent to D₂O/CD₃CN and a longer scan time improved resolution (Figure 29). Whilst the resolution was still less than ideal the key regions relating to **PDI-2** could be identified. The four characteristic aromatic core peaks of **PDI-2** (red: 8.75, 8.59, 8.42 and 8.12 ppm) as well as the two doublets for the aryl group adjacent to the phosphorus (purple: 7.92 and 7.81 ppm), followed by the hydrogens associated with the carbon between the phosphorus and imide position (orange: 4.27 ppm), then the alky groups from the stopper group (green: 1.81-15.3 ppm) and finally the terminal methyl groups (blue: 1.28 and 1.23 ppm). The location of all key peaks supports addition of **PDI-2** to **P₂W₁₇** (Figure 29).

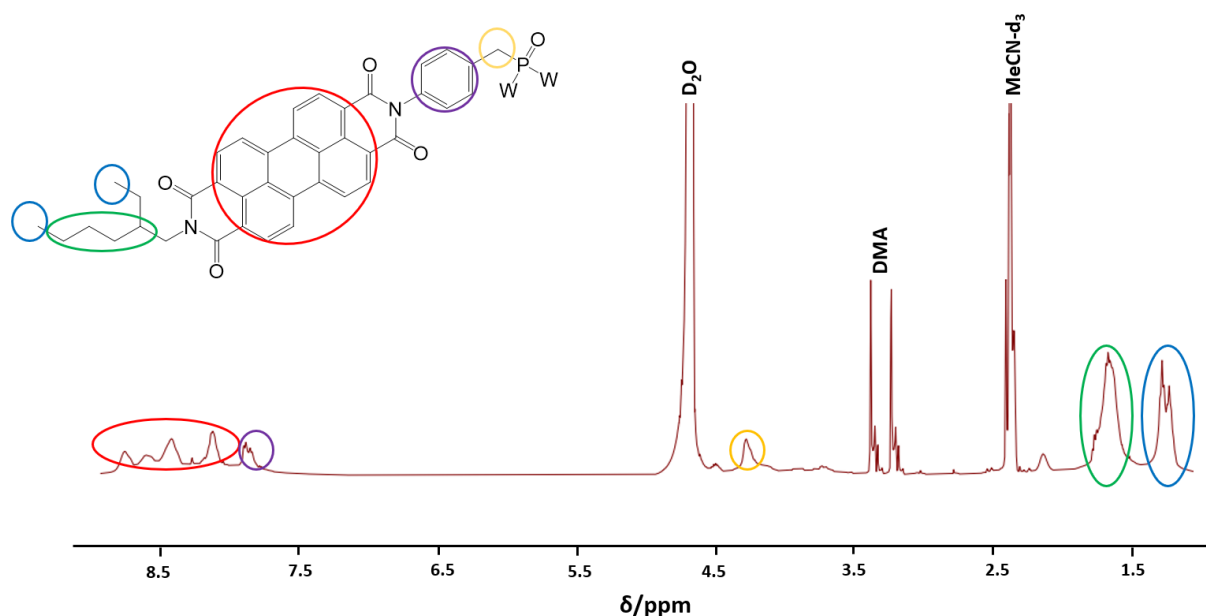


Figure 29: ¹H NMR spectrum of PDI-POM in D₂O/MeCN-d₃ (1:1) List of peaks: δ 8.75 (s, 2H), 8.59 (s, 2H), 8.42 (s, 2H), 8.12 (s, 2H), 7.92–7.81 (m, 4H), 4.27 (s, 2H), 1.81 – 1.53 (m, 8H), 1.31 – 1.25 (t, 3H), 1.23 (t, 3H). Key areas of PDI ligand have been highlighted: aromatic core (red), aryl ring (purple), hydrogens adjacent to phosphorus (orange), alkyl chain (green) and terminal methyl groups (blue)

As with the characterisation of P_2W_{18} and P_2W_{17} , analysis of the phosphorus environments through ^{31}P NMR spectroscopy provided valuable insight into the materials structure. The hybrid POM should contain two distinct phosphorus environments corresponding to the two hetero PO_4 units (peaks should occur at negative ppm) within the POM structure and one peak related to the ligand's phosphorus linker (the peak should occur at positive ppm). Surprisingly six distinct peaks were observed (Figure 30), two peaks were seen at positive chemical shifts (26.13 and 20.34 ppm) and four at negative shifts (-10.04, -10.11, -12.57 and -12.71 ppm). The arrangement of the peaks hint at two distinct hybrid species, all the peaks are shifted from the ligand and P_2W_{17} values combined with both precursors' poor solubility in MeCN suggests the extra peaks do not correlate with the starting materials.

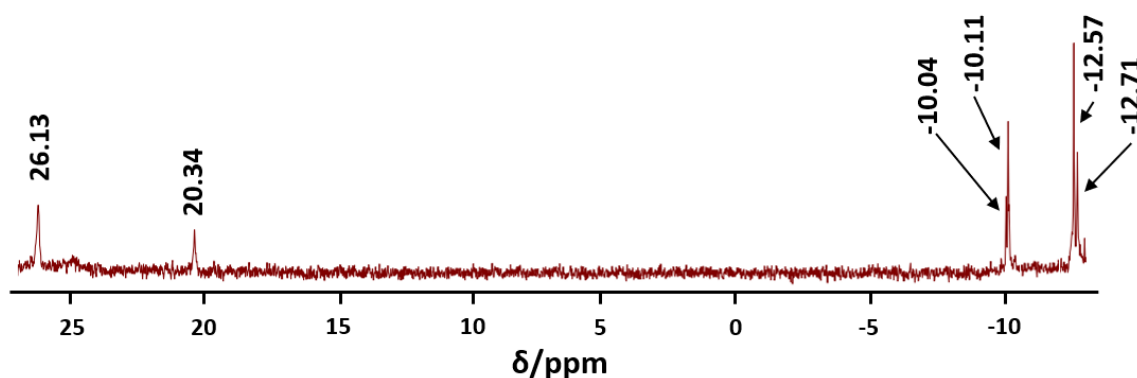


Figure 30: ^{31}P NMR spectrum for PDI-POM in MeCN- d_3 . List of peaks with their splitting and J coupling (Hz): ^{31}P NMR (162 MHz, CD_3CN) δ -10.04, -10.11, -12.57, -12.71.

Further purification of the material through a mixture of solvent washes was unsuccessful suggesting the two hybrids have near indistinguishable solubility. An attempt to grow single crystals was made through diffusion crystallisation, with the goal to provide an X-ray crystal structure and separate the two materials. For the crystallisations the samples were dissolved in a minimum of DMF or MeCN, a

range of anti-solvents were tested (MTBE, CHCl₃, Et₂O, THF, MeOH) however crystals suitable for X-ray crystallography were unable to be produced.

ESI-MS was used to provide further insight into the structure of the material (Figure 31). The expected formula for the hybrid was [P₂W₁₇O₆₁(C₃₉H₃₁N₂O₅P)₂]⁶⁻, this anion was located with ESI-MS (Table 4). ESI-MS also causes fragmentation of the molecule, the fragments corresponding to the loss of one ligand was also located. This data helps improve confidence that the hybrid was formed supporting the peaks seen in NMR spectroscopy.

Table 4: Selected ESI MS assignments for PDI-POM

Assignment	Z	m/z (calc)	m/z (obs)
{H ₃ [P ₂ W ₁₇ O ₆₁ (C ₃₉ H ₃₁ N ₂ O ₅ P) ₂]} ³⁻	3-	1814.08	1814.11
{H ₂ Na [P ₂ W ₁₇ O ₆₁ (C ₃₉ H ₃₁ N ₂ O ₅ P) ₂]} ³⁻	3-	1821.72	1821.72
{HNa ₂ [P ₂ W ₁₇ O ₆₁ (C ₃₉ H ₃₁ N ₂ O ₅ P)]} ³⁻	3-	1616.33	1616.33
{Na ₃ [P ₂ W ₁₇ O ₆₁ (C ₃₉ H ₃₁ N ₂ O ₅ P)]} ³⁻	3-	1623.66	1623.65

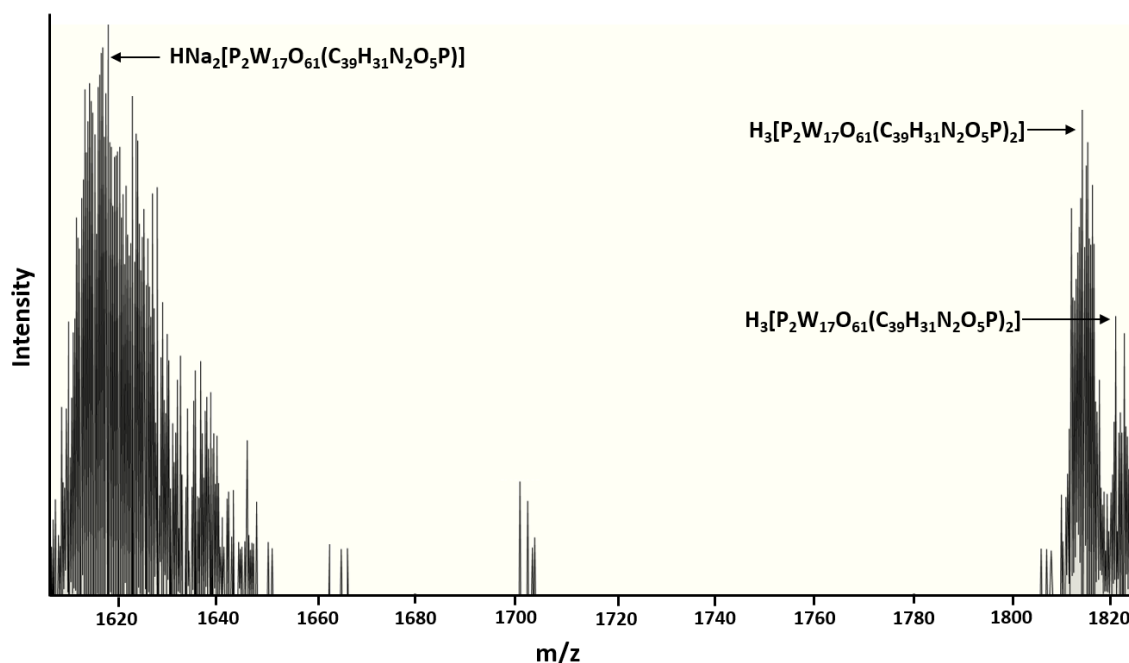


Figure 31: A section of the ESI mass spectrum for PDI-POM in the range of 1600-1840 m/z. Key fragments have been annotated.

Thermogravimetric analysis (TGA) was applied on the hybrid material to gain further insight into its composition (Figure 32). After equilibration at 30 °C a steady decline in weight loss occurred finishing at 747.20 °C, this weight loss correlates to the weight of the counter ions and organic components. The expected formula based on our knowledge of Well-Dawson hybridisation and the MS finding for the hybrid is $[P_2W_{17}O_{61}(C_{39}H_{33}N_2O_5P)_2]^{6-}$, the most likely counter ions are potassium as a large excess was involved in the hybridisation step.^{34, 43} The potassium counter ions and PDI ligands account for 26.61% of the total weight, the TGA results support this as 26.56% weight was lost during the analysis. The remaining weight can be attributed to the core POM structure.

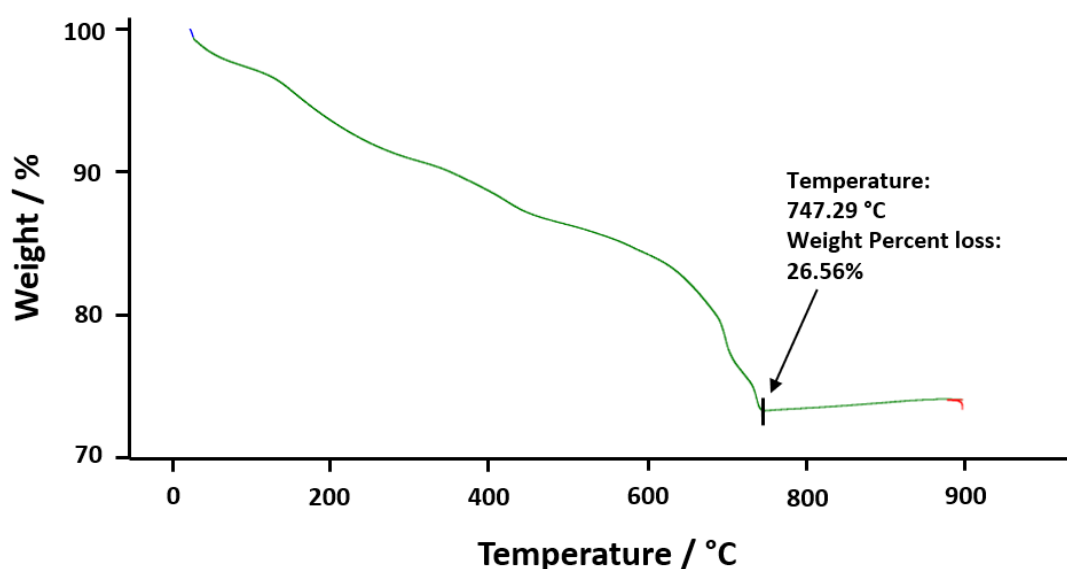


Figure 32: Thermogram for PDI-POM. Equilibration temperature at 30 °C, with a ramp time of 5 °C per min up to 1000 °C with a 10 min isothermal. 26.561% weight loss observed.

The combined data of NMR spectroscopy, MS and TGA support successful hybridisation of P_2W_{17} and **PDI-2**. From the MS data the anions for the expected target material $[P_2W_{17}O_{61}(C_{39}H_{31}N_2O_5P)_2]^{6-}$ have been located. As hypothesised potassium would be the most likely counter ion for this anion and the TGA weight percentages suggests that this is the case. With this data we can propose the most likely

formula for the new hybrid material is $K_6[P_2W_{17}O_{61}(C_{39}H_{33}N_2O_5P)_2]$ (hereafter referred to as **PDI-POM**, Figure 33).

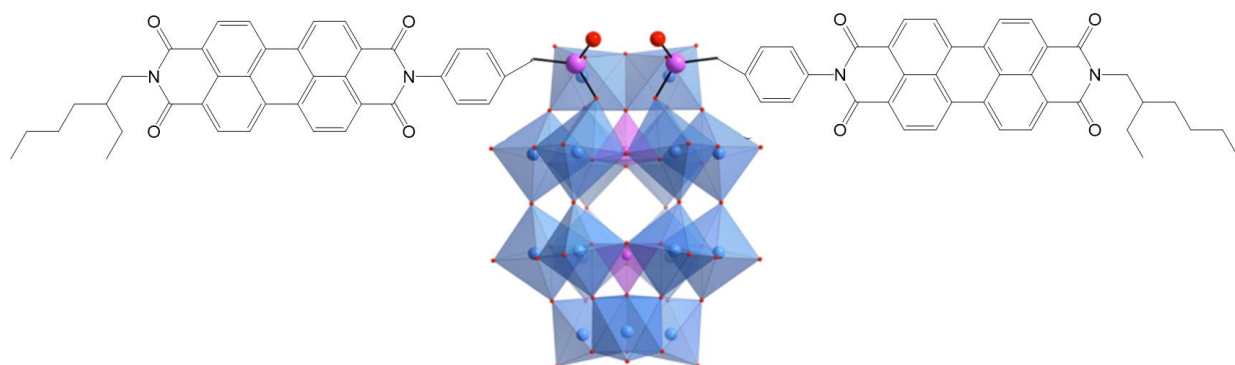


Figure 33 Structure of the Wells-Dawson polyoxometalate covalently functionalized with asymmetric perylene ligands (**PDI-POM**).

3.4 Spectroscopic Analysis of the Polyoxometalate Hybrid

3.4.1 Infrared Spectroscopy

To further probe the bonding and characterise the new hybrid material IR spectroscopy was applied (Figure 34). The fingerprint region for POMs displays several distinctive features. A broad band in the range of $600-800\text{ cm}^{-1}$ observed in both the hybrid and P_2W_{17} corresponds to the W-O-W bending mode of the bridging oxygens, additional peaks at 908 cm^{-1} and 947 cm^{-1} are assigned to the W=O stretching modes. Following this the peaks observed at 1084 cm^{-1} relate to the P-O and P=O of the internal phosphates of the POM and the ligand linker. Compared to P_2W_{17} extra peaks are observed in the range of $1250-1500\text{ cm}^{-1}$, the more complicated fingerprint region supports the addition of an organic functionality. The hybrid displays peaks at 1346 cm^{-1} assigned to the C-N stretch and 1695 cm^{-1} for the C=O stretching modes. The most distinguishable of these ligand peaks are seen at 2860 cm^{-1} and 2929 cm^{-1} . These are assigned to the C-H symmetric and antisymmetric stretching modes respectively, resulting from the C-H bonds in the aromatic ring of the PDI. Overall IR spectroscopy

supports the addition of **PDI-2** to P_2W_{17} with key features from both materials being observed in the hybrid.

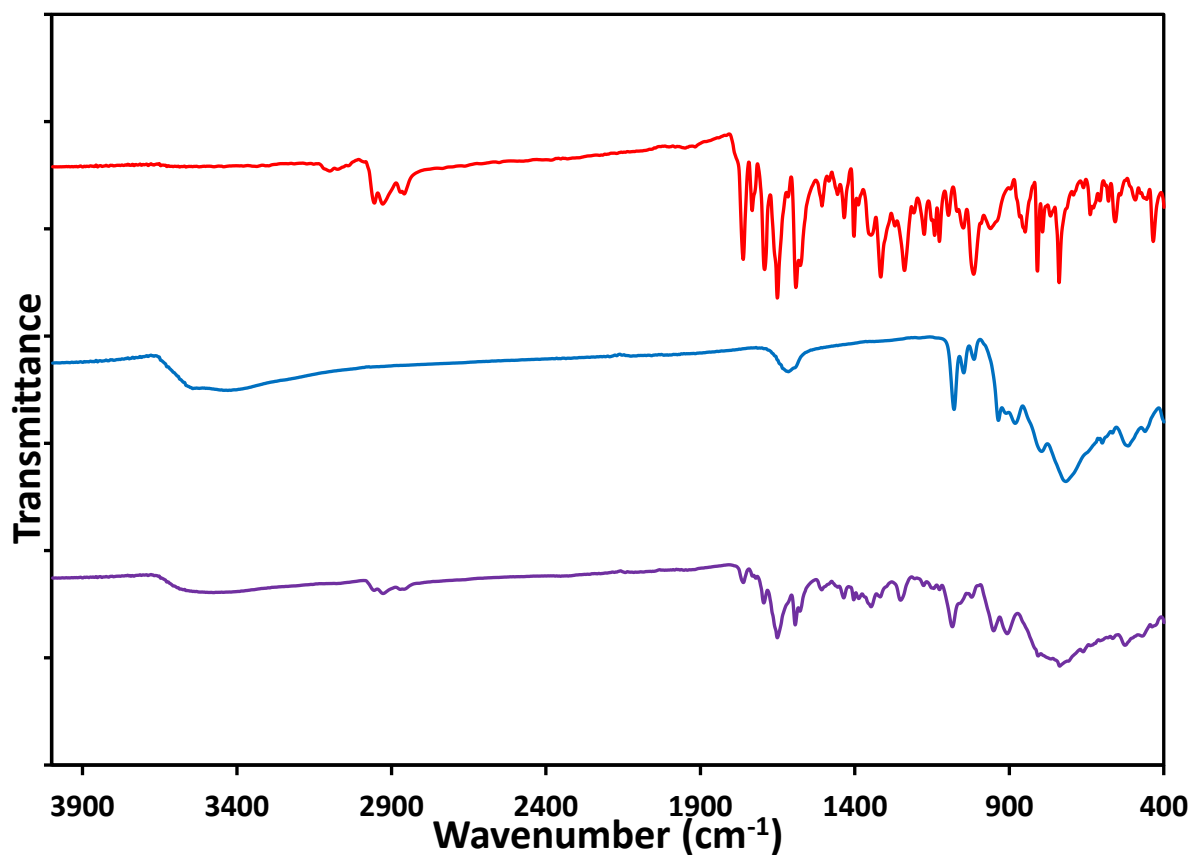


Figure 34: An FT-IR ATR spectrum of PDI-1 ligand (red) overlaid with P_2W_{17} (blue) and PDI-POM (purple)

3.4.2 Ultraviolet Visible Spectroscopy

Additionally, UV-vis spectroscopy was employed to investigate the absorbance of the new hybrid material (Figure 35). In the case of POMs their primary absorbance can be attributed to the LMCT from $O \rightarrow W$, this occurs in the near UV region typically < 400 nm. As expected, the spectra of P_2W_{17} shows no absorbance until 370 nm, after which strong absorbance is observed confirming the strong UV absorbance properties of POMs. The UV spectra for **PDI-1** displays the characteristic three peaks observed by PDIs. Two distinct absorption bands are seen at 525 nm and 492 nm followed by a broad shoulder at 459 nm, these peaks correspond to the $0 \rightarrow 0$, $0 \rightarrow 1$ and $0 \rightarrow 2$ vibronic transitions.⁵⁵ **PDI-**

POM shows the characteristic LMCT band expected of POMs, an additional near UV absorbance peak at 387 nm exists also observed in **PDI-1**. Prominent absorption peak characteristics of the PDI vibronic structure are also observed in the hybrid material at 527 nm, 492 nm, and 459 nm. The bands occur at equivalent wavelengths to **PDI-1**, this is not unexpected as there should be minimal change in the PDIs electronic character upon hybridisation due to the node in the imide position. A significant increase in absorbance is observed by the hybrid particularly in the 550-420 nm range. This is rationalised by **P₂W₁₇** having four exposed oxygen centres that can accommodate two phosphate ligands. The di-functionalised hybrid contains two PDI ligands per mole of hybrid causing enhanced absorption. Probing the hybrid with UV-vis spectroscopy clearly show the characteristic strong peaks in the visible light region of the spectra corresponding to those of **PDI-1**. The new absorbance bands combined with amplified absorbance provides further evidence for successful hybridisation of **PDI-POM** as well as being promising characteristics for a photocatalytic material.

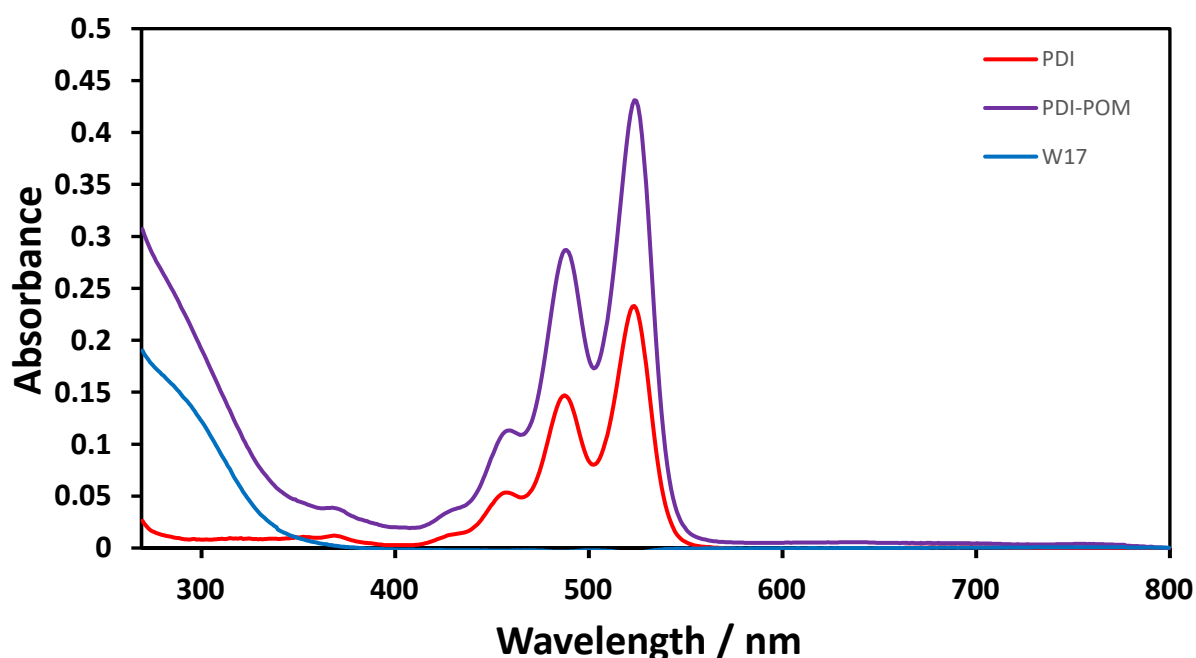


Figure 35: UV-vis spectra for PDI-1 (red), **P₂W₁₇** (blue) and PDI-POM (purple). Solution was prepared at 4×10^{-6} M concentration.

3.4.3 Fluorescence Spectroscopy

As described above, perylene chromophores display strong fluorescence. It is expected that both **PDI-1** and **PDI-POM** will show distinctive emission spectra when analysed using solution phase fluorimetry. From the UV-Vis absorbance spectroscopy we know that both species maximum absorbance occurs at 525 nm. The excitation wavelength was selected just below the absorbance maximum at 520 nm, this was expected to provide the best emission spectra.

Figure 36 shows the emission spectra of **PDI-POM** overlaid with its absorption spectra (the absorbance and emission values have been normalised). Characteristic of fluorescence spectra is to be a mirror image of the absorbance spectra; this is because the transitions that are most favourable for absorbance will also be the most favourable for emission. From Figure 36 we can see the vibronic structure ($0 \rightarrow 0$, $0 \rightarrow 1$, $0 \rightarrow 2$) clearly, with the final transition appearing as a broad shoulder peak. The energy loss that occurs in the excitation luminescence cycle from the transition between vibrational levels causes the emitted photon to be lower energy than the absorbed one and therefore emitted at a higher wavelength. This phenomenon is known as the Stokes shift and is also observed in the spectra of **PDI-POM**, the spectra is red shifted with a Stokes shift of 21 nm.

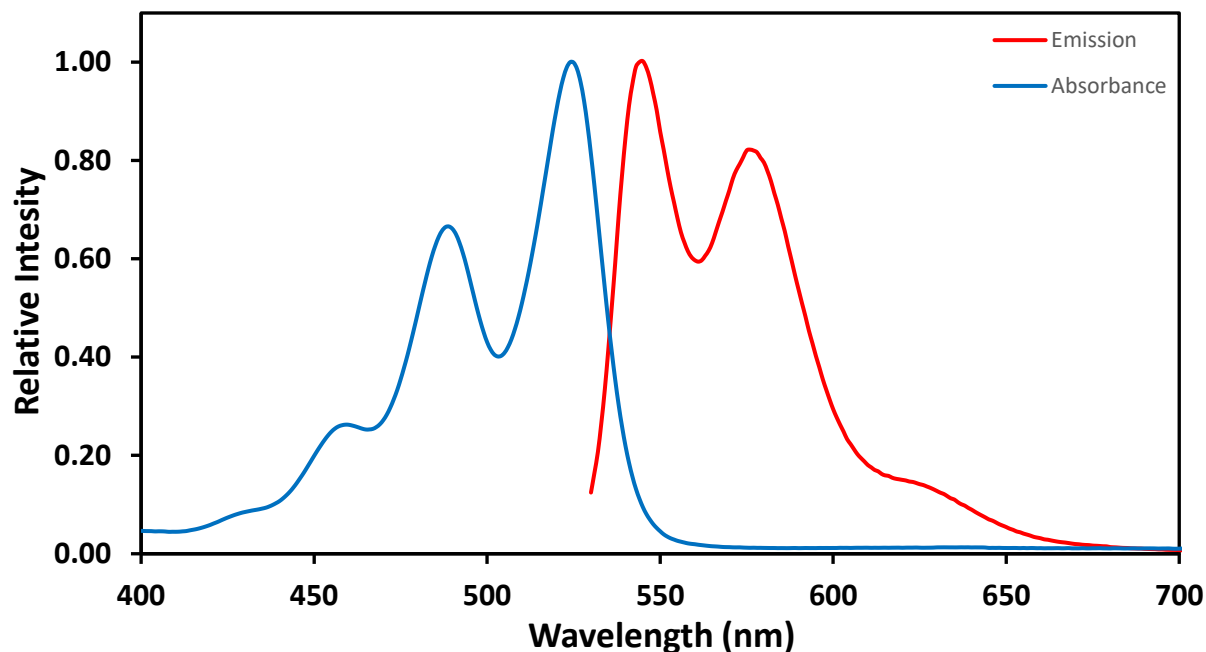


Figure 36: Fluorescence (red) and UV-vis (blue) spectra for PDI-POM. Spectra have been normalised to the most intense peak.

Comparison of the emission spectra of both species is shown in Figure 37. As with their maximum absorbance **PDI-1** and **PDI-POM** show a similar maximum emission at 542 nm and 546 nm respectively, **PDI-1** has significantly higher emission detected at a maximum of 4.08×10^7 counts per second (CPS) detected. The lower maximum emission observed in **PDI-POM** at 1.05×10^7 CPS is indicative of effective intermolecular charge transfer from the excited perylene ligands to the POM core, resulting in quenching emission. Furthermore, **PDI-POM** contains twice the amount perylene units per mole of compound compared to **PDI-1**, if we normalise the emission to take this into account (5.25×10^6 CPS) then we observe that the maximum emission has been quenched by 87.13%. This supports the findings by Zhang, Li and Harriman who also observed significant fluorescence quenching in their perylene-POM hybrids.^{44, 45, 47}

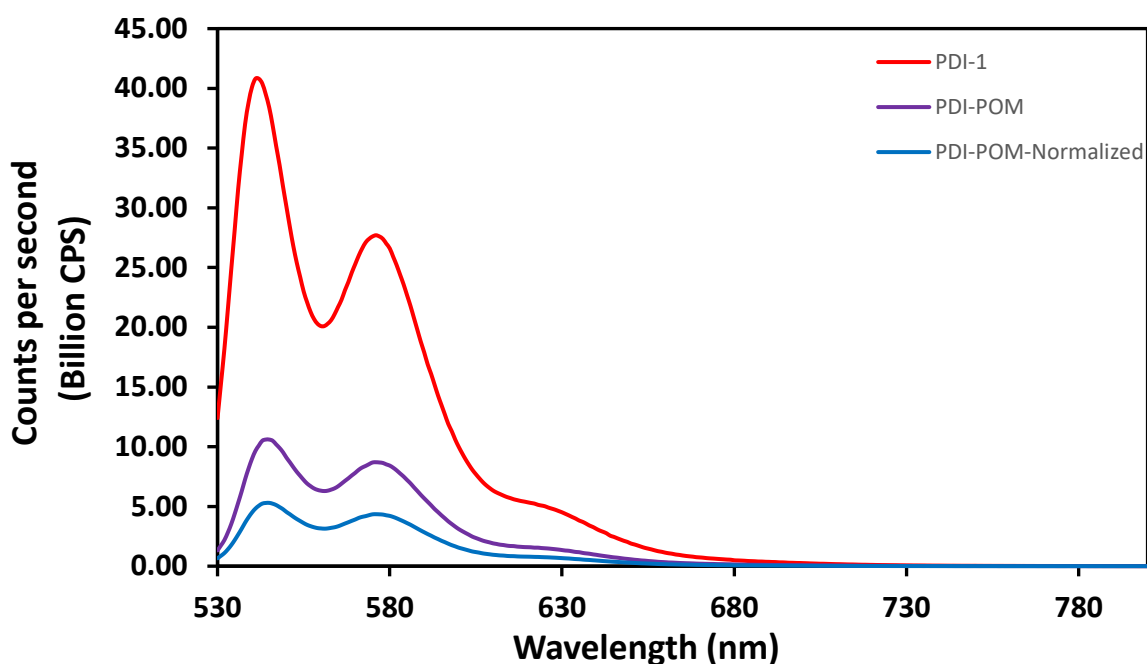


Figure 37: Fluorescence emission spectra of PDI-1 (red) and PDI-POM (purple) at an excitation wavelength of 520 nm. Normalised data for PDI-POM (blue) has been included, normalised to the number of perylene units per mole of compound.

3.5 Electrochemistry

The electrochemical properties of the new hybrid material and its parent compounds were examined. Cyclic voltammetry (CV) was used to determine the nature and number of redox processes for the POM species and the PDI chromophore. $\mathbf{P}_2\mathbf{W}_{18}$ was analysed by cyclic voltammetry instead of $\mathbf{P}_2\mathbf{W}_{17}$, despite the lacunary POM and hybrid having the same overall charge $\mathbf{P}_2\mathbf{W}_{17}$ has an exposed lacunary site whereas both the hybrid and $\mathbf{P}_2\mathbf{W}_{18}$ have the site occupied (W=O unit occupies $\mathbf{P}_2\mathbf{W}_{18}$ site and **PDI-2** occupies **PDI-POM**) and it was hypothesized the redox behaviour of $\mathbf{P}_2\mathbf{W}_{18}$ and **PDI-POM** would be more similar.

It was important to select a solvent that would not only dissolve all three compounds but also be stable within the potential window for POM and perylene redox processes. The primary redox activity of both POMs and PDIs predominantly occurs at negative potentials.⁷⁴⁻⁷⁶ Hence DMF was selected as an ideal solvent due to good solubility for all compounds and a solvent window that lies between 1.6 and -2.8 V, allowing for full exploration of potential redox processes.⁷⁷ All CVs were set up with 0.1 M

solutions of $[\text{Bu}_4\text{N}][\text{PF}_6]$ as the electrolyte and degassed with argon for 15 mins to remove oxygen which is redox active and would display distinct peaks in the CVs. A scan rate of 100 mVs^{-1} was used to measure the $E_{1/2}$ and peak currents (I_p) and all CVs were referenced vs. ferrocenium/ferrocene (Fc^+/Fc).

P_2W_{18} shows four quasi reversible redox processes with $E_{1/2}$ calculated as -1158 mV , -1403 mV , -1741 mV and -1985 mV vs. Fc^+/Fc . The ratio of I_p for the four redox couples is $\sim 1:1:2:2$ suggesting two $1e^-$ processes followed by two $2e^-$ processes which is characteristic of P_2W_{18} . The potential of the $E_{1/2}$ values for all peaks was found to be independent of scan rate suggesting the redox couples are reversible. In addition, I_p of the first oxidation was found to be directly proportional to the square root of scan rate ($(\text{Vs}^{-1})^{1/2}$) signifying a diffusion controlled process and reversible electron transfer (Figure 38).⁷⁸ Two quasi-reversible redox processes were observed for **PDI-1**, $E_{1/2}$ values were measured as -868 mV and -1120 mV vs. Fc^+/Fc . As with P_2W_{18} no significant shift in peak shape or potential was observed with increasing scan rate and a linear relationship was observed between I_p and $(\text{Vs}^{-1})^{1/2}$ suggesting good electrochemical reversibility. The two $1e^-$ processes observed are characteristic of PDIs and fall within the expected potential range.⁷⁹

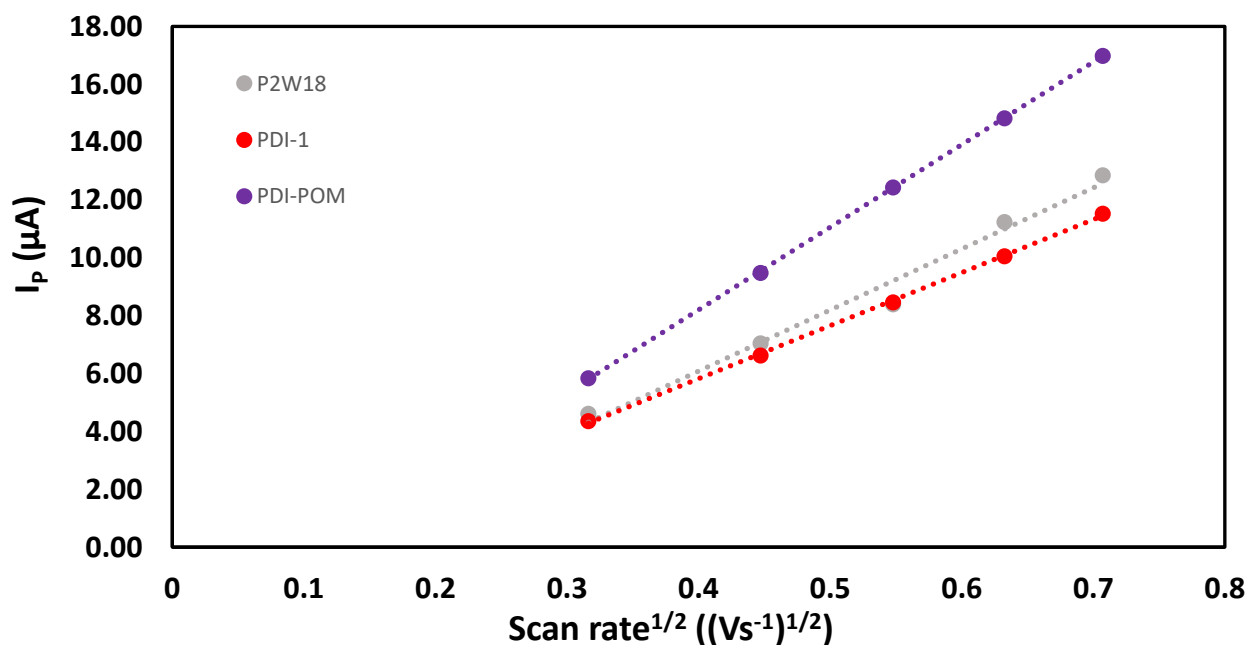


Figure 38: Plot of I_p for the first oxidation of the hybrid material and its precursors against the square root of scan rate. P_2W_{18} : Grey, PDI-1: Red, PDI-POM: Purple.

Examination of **PDI-POM** with CV showed four quasi-reversible redox processes with $E_{1/2}$ values calculated as -9270 mV, -1125 mV, -1528 mV and -1977 mV vs. Fc^{+}/Fc (Table 5). **PDI-POM** was also studied under five increasing scan rates from 100-500 mVs^{-1} , no significant shift in potential or peak shape occurred and once more a linear relationship was also observed for i_p vs $(Vs^{-1})^{1/2}$, suggesting a reversible processes.

Table 5: Redox potentials for PDI-POM referenced vs. Fc^{+}/Fc (V)

Redox potentials vs. Fc^{+}/Fc (V)	I	II	III	IV
E_{red}	-0.949	-1.153	-1.581	-2.041
E_{ox}	-0.905	-1.097	-1.475	-1.913
$E_{1/2}$	-0.927	-1.125	-1.528	-1.977

Figure 39 overlays the CVs for **PDI-POM** and its precursors, process I and II fall within the region of perylene redox processes and can be attributed to the PDI ligands. Process III and IV correspond to the POM redox couples, as the key redox processes of both precursor materials are observed in **PDI-POM** we have further confirmation of successful hybridisation and can see the redox chemistry of both species is retained. Process III and IV have been positively shifted by 213 mV and 8 mV. This agrees with the literature where the electron withdrawing effect of organophosphate ligands positively shifts reduction potentials.²⁷

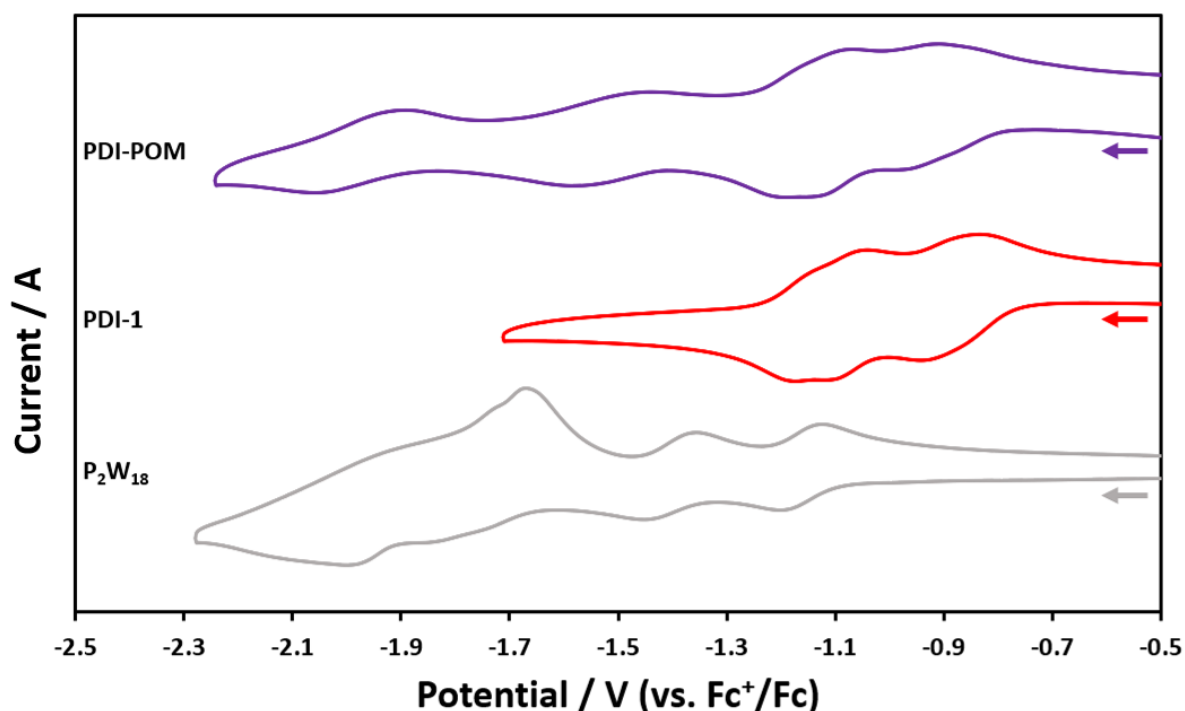


Figure 39: Cyclic voltammograms of polyoxometalate hybrid and its precursor materials in DMF containing 0.1M [Bu₄N][PF₆] as the supporting electrolyte, with a scan rate of 100 mVs⁻¹. Purple: PDI-POM, Red: PDI-1, Grey: P₂W₁₈

It is also possible that a further two redox processes exist in **PDI-POM**, as we know there are normally four redox couples associated with **P₂W₁₈** however only two processes ascribed to the POM moiety are observed. In the work of Odobel et al. they found an overlap of the POM and perylene potentials within their hybrid materials.⁴⁷ It is possible that hybridisation positively shifts the POM precursors first and second redox couples enough to be totally obscured by the PDI processes, hence six or more processes may exist in **PDI-POM**. To further explore this concept the redox properties of the PDI ligand could be tweaked, incorporating electron withdrawing groups to the PDI core would induce a positive shift in its redox potentials potentially revealing new hybrid redox couples. Overall, the positive shift in **PDI-POMs** redox potentials suggests interaction between the ligand and the POM core potentially due to intermolecular electron transfer.

4. Conclusions and Future Work

A novel polyoxometalate hybrid has been produced based on a mono lacunary Wells-Dawson structure. Careful consideration was made in designing an asymmetric PDI that would impart the best chemical, electrochemical and physical properties to the hybrid. The new material was characterised by complimentary ^1H , ^{13}C and ^{31}P NMR spectroscopy combined with mass spectrometry, TGA and IR analysis. The optical and electrochemical properties were probed using UV-vis spectrometry, fluorimetry and cyclic voltammetry.

Whilst ^{31}P NMR spectroscopy raises some questions as to the purity of the final product, we can be confident that one set of peaks belongs to the target hybrid ($\text{K}_6[\text{P}_2\text{W}_{17}\text{O}_{61}(\text{C}_{39}\text{H}_{33}\text{N}_2\text{O}_5\text{P})_2]$). A combination of supporting evidence including ^1H NMR spectroscopy, MS, IR spectroscopy, and UV-vis spectroscopy all suggest successful hybridisation of the lacunary Wells-Dawson with **PDI-1**. It is possible that the additional peaks occur from solution phase behaviour of the material such as tautomerism or could be a side reaction occurring during hybridisation. Future work would look to further purify and locate the origin of these peaks. Strong visible light absorptions at 526 nm supports addition of the asymmetric PDI to the POM. Furthermore, both the electrochemical analysis which showed shifted redox potentials and fluorescence quenching observed through fluorimetry suggests intermolecular charge transfer from the PDI unit to the POM.

Due to time restrictions, certain characterisation methods were unable to be completed, primarily elemental analysis would be core to further confirming the composition of **PDI-POM**. Producing a crystal structure by growing suitable single crystals was attempted by diffusion crystallisation, however, ideal conditions for crystallisation were not found. Varying solvent combination as well as diffusion times and crystallisation methods could help produce crystals suitable for use in X-ray crystallography, producing a full crystal structure and purify the material further. Charge transfer mechanics of the PDI to the POM could also be probed with time resolved fluorescence lifetime experiments, observing shorter fluorescence lifetimes would correlate with rapid charge transfer from

the PDI to the POM. The final goal of designing this material is use in photocatalytic reactions, attempting to reproduce catalytic experiments seen within the literature using **PDI-POM** would be extremely beneficial. If improved catalytic turnover is observed, it would support the observations made through spectroscopic and electrochemical analysis that suggest intermolecular charge transfer is occurring in **PDI-POM**.

Future work could also consider expanding the library of hybrid PDI-POM materials. The PDI unit could be modified in several ways to continue to adapt its properties. Modification to the bay area seems to be the logical next step, this would allow fine tuning of the electronic and optical properties of the PDI. Analysing the observed properties of the new hybrid POMs would help further confirm the synergy between the PDI and POM, if shifts occur in its absorption, emission, and redox properties it can be assumed the PDI ligand is having a direct effect on the POM. One of the major hurdles in characterising and synthesising the perylene derivatives was their poor solubility. Further exploration into the available 'swallow tail' alkanes and bulky aromatics could look to find groups that better solubilise the final PDI product. To investigate the electron transport properties of PDIs to the POM core different organic linkers could be used. Investigating the effect of using an alkyl chain between the perylene and phosphorus linker instead of an aryl ring and modulating the chain length could enhance electron transport properties. Also, the type of X group in the M-O-X linkage being changed to Si, S or Sn groups could also adapt these properties.

The first steps in producing a covalent PDI-POM hybrid have been successful and show promising properties suggesting intermolecular charge transfer and visible light sensitivity. This project has looked to give a first insight into the potential of asymmetric perylenes in POM photocatalysts, however, there is clearly more opportunities to fully optimize the synthetic procedure and explore the intricacies of molecular design for producing new hybrid catalytic materials.

5. Experimental

5.1 Materials and Instrumentation

All reagents and solvents were purchased from Thermo Fisher Scientific, Alfa Aesar and Sigma Aldrich and used without further purification.

^1H NMR, ^{13}C NMR and ^{31}P NMR spectra were obtained using a 400 MHz Bruker AV400 or 500 MHz Bruker AV(III) 500 spectrometer at 298K. Chemical shifts (δ) are recorded in parts per million (ppm). Peak multiplicity is denoted by the following abbreviations: singlet (s), doublet (d), triplet (t), quartet (q) and multiplet (m) with coupling constants (J) given in Hertz (Hz).

Attenuated Total Reflection Fourier-transform Infra-red spectroscopy (ATR-FTIR) was recorded in the 400-4000 cm^{-1} range using a Bruker Tensor 27 spectrometer equipped with a Pike GladiATR module with a diamond crystal.

UV-vis spectroscopy was performed in quartz glass cuvettes using an Agilent Cary 5000 UV-Vis-NIR Absorption spectrometer.

Fluorescence spectra were recorded using a quartz fluorescence cuvette, with a 1 cm path length on an Edinburgh Instruments FLS980 Photoluminescence spectrometer with an excitation wavelength of 520 nm.

Electrospray ionisation mass spectrometry (ESI-MS) was performed on Bruker MicroTOF and Impact II spectrometers operating in negative mode. Samples were prepared for analysis by dissolving ~ 1 mg of solid in HPLC grade acetonitrile and introduced to the spectrometer via an autosampler which injected 20 μL of the sample into a stream of 70:30 v/v MeOH/H₂O. Data was analysed on the Bruker Compass Data Analysis software suite. Modified instrument parameters were used for detection of high molecular weight polyoxometalate anions

Matrix-assisted laser desorption/ionization mass spectrometry (MALDI-MS) were recorded with a Bruker Ultraflex III mass spectrometer in positive mode.

Thermogravimetric Analysis (TGA) were performed using TA-Q500 (TA Instruments) using a high temperature platinum pan. TGA was equilibrated at 30 °C and a ramp of 5 °C per minute up to 1000 °C with an isothermal at 1000 °C for 10 mins under air flow streams.

Cyclic Voltammetry was performed on CHI600E (CH Instruments) workstation for solution state measurements. A standard three electrode set up was used for all measurements: working electrode (glassy carbon, d = 3mm), counter electrode (Pt wire) and reference electrode (Ag wire). Experiments were performed in an electrolyte solution of [Bu₄N][PF₆] (0.1 M, 10 mL) in dry DMF. All potentials were referenced against an internal standard of ferrocenium/ferrocene (Fc⁺/Fc). Initial CV experiments were performed at a scan rate of 100 mVs⁻¹ and increased to 500 mVs⁻¹ in increments of 100 mVs⁻¹.

5.2 Synthesis of Asymmetric PDIs

Synthesis of asymmetric PDIs was completed following an adapted method reported by Xue et al⁶⁹

5.2.1 Synthesis of 3,4,9,10-tetra(decyloxycarbonyl)perylene (PTE)

PTCDA (7.84 g, 20 mmol) was added to a stirred solution of KOH (6 g, 107 mmol) and deionised water (100 mL). The solution was heated to 70 °C for 1 h. The solution was filtered and HCl (1.0 M) was added until pH 8 was reached. To the filtrate aliquot 336 (2.7 g, 6.7 mmol) and KI (0.5 g, 3 mmol) was added and stirred vigorously for 10 mins. To the stirred solution decyl bromide (35.4 g, 160 mmol) was added and refluxed for 2 h. The product was extracted with CHCl₃ (250 mL) and washed with aqueous NaCl solution (3 x 100 mL, 15% w/v). Addition of methanol precipitated the product as an orange solid which was collected via filtration and air dried (16.84 g, 85%). ¹H NMR (400 MHz, CDCl₃) δ 8.26 (d, J = 8.0 Hz, 4H), 8.03 (d, J = 7.9 Hz, 4H), 4.32 (t, J = 6.9 Hz, 8H), 1.79 (p, J = 7.0 Hz, 8H), 1.50 – 1.39 (m, 56H), 0.88 (td, J = 6.9, 2.5 Hz, 12H); IR (ATR): 2953, 2914, 2849, 1732, 1712, 1589, 1467, 1269, 1155, 1151, 1008 cm⁻¹; MS (MALDI)⁺ m/z 988.770 (C₆₄H₉₂O₈: [M]⁺ requires 989.41).

5.2.2 Synthesis of Perylene-3,4-anhydride-9,10-di(decyloxy carbonyl) (**PDE**)

A solution of PTE (3.983 g, 4.03 mmol), toluene (1.5 mL) and n-dodecane (6.75 mL) was heated to 90 °C. To the hot solution P-toluene sulfonic acid (0.766 g, 4.03 mmol) was added and refluxed for 5 h. The dark red gelatinous solution was extracted with CHCl₃ (100 mL) and mixed with silica gel. This was purified by column chromatography (silica, 50:1 chloroform: acetone) producing a sticky red solid (1.792g, 64%). ¹H NMR (400 MHz, CDCl₃) δ 8.59 (d, *J* = 7.9 Hz, 2H), 8.44 (d, *J* = 7.9 Hz, 2H), 8.10 (d, *J* = 7.8 Hz, 4H), 4.36 (t, *J* = 6.9 Hz, 4H), 1.84 (p, *J* = 7.1 Hz, 4H), 1.64 – 1.53 (m, 4H), 1.53 – 1.23 (m, 24H), 0.90 (t, *J* = 6.7 Hz, 6H); IR (ATR): 2953, 2922, 2852, 1768, 1730, 1708, 1595, 1407, 1286, 1253, 1151, 1126 cm⁻¹; MS (MALDI)⁺ *m/z* 690.437 (C₄₄H₅₀O₇: [M]⁺ requires 690.86).

5.2.3 Synthesis of *N*-(2-ethylhexylamine)-perylene-3,4-dicarboximide-9,10-di(decyloxy carbonyl)(**PMIDE**)

PDE (300 mg, 0.434 mmol) was dissolved in neat ethyl hexylamine (5 mL) and was heated at 120 °C for 16 h under Ar atmosphere. The reaction mixture was cooled to room temperature then extracted with CHCl₃ (50 mL) and adsorbed onto silica gel. This was purified by column chromatography (silica, 40:1 chloroform: acetone) producing a bright red solid (168 mg, 67%). ¹H NMR (400 MHz, CDCl₃) δ 8.58 (d, *J* = 8.0 Hz, 2H), 8.45 – 8.37 (m, 4H), 8.08 (d, *J* = 7.9 Hz, 2H), 4.34 (t, *J* = 6.9 Hz, 4H), 2.01 – 1.93 (m, 1H), 1.81 (p, *J* = 7.0 Hz, 4H), 1.54 (s, 4H), 1.51 – 1.17 (m, 30H), 0.95 (t, *J* = 7.4 Hz, 3H), 0.88 (t, *J* = 7.0 Hz, 3H); IR (ATR): 2958, 2922, 2852, 1720, 1699, 1655, 1593, 1298, 1263, 1170, 1070 cm⁻¹; MS (MALDI)⁺ *m/z* 802.60 (C₅₂H₆₇NO₆: [M]⁺ requires 802.09).

5.2.4 Synthesis of *N*-(2-ethylhexylamine)-perylene-3,4-dicarboximide-9,10-anhydride (**PMI**)

A stirred solution of PMIDE (200 mg, 0.25 mmol) and toluene (15 mL) was brought to 90 °C. To the hot solution P-toluene sulfonic acid (95 mg, 0.5 mmol) was added and refluxed for 16 h. A copper-coloured precipitate formed and was collected by centrifugation and washed with methanol. (116 mg, 93%). IR

(ATR): 3105, 2954, 2924, 2858, 1761, 1759, 1689, 1651, 1589, 1404, 1351, 1234, 1124, 1012 cm^{-1} ; **MS**

(MALDI)⁺ m/z 503.214($\text{C}_{32}\text{H}_{25}\text{NO}_5$: [M]⁺ requires 503.54).

5.2.5 Synthesis of *N*-(2-ethylhexylamine)-*N'*-(diethyl 4-aminobenzylphosphonate)-perylene-3,4,9,10-tetracarboxylic diimide (**PDI-1**)

PMI (200 mg, 0.397 mmol) and diethyl 4-aminobenzylphosphonate (193 mg, 0.794 mmol) were added to a flask under Ar atmosphere. To the flask dry DMF (20 mL) was added and was heated to 120 °C for 72 h. The reaction was cooled to room temperature and solvent removed by evaporation in vacuo. The crude solid was redissolved in CHCl_3 (100 mL) and washed with deionised water (3 x 100 mL), the organic layer was dried over MgSO_4 , and the solvent was removed. The crude solid was purified by column chromatography (silica, 20:1 ethyl acetate: methanol) producing a red solid (214 mg, 74%).

λ_{max} (abs) = 526 nm; ¹H NMR (400 MHz, CDCl_3) δ 8.66 (d, J = 7.9 Hz, 2H), 8.56 (d, J = 7.9 Hz, 2H), 8.50 (d, J = 8.1 Hz, 2H), 8.45 (d, J = 8.1 Hz, 2H), 7.56 – 7.49 (m, 2H), 7.36 (d, J = 7.8 Hz, 2H), 4.10 (dq, J = 14.7, 7.5 Hz, 4H), 3.32 – 3.23 (m, 2H), 1.99 – 1.88 (m, 1H), 1.62 (s, 2H), 1.44 – 1.17 (m, 12H), 0.95 (t, J = 7.3 Hz, 3H), 0.92 – 0.84 (m, 3H); ³¹P NMR (162 MHz, CDCl_3) δ 25.82; **IR** (ATR): 3101, 2956, 2929, 2860, 1761, 1695, 1651, 1591, 1402, 1350, 1317, 1236, 1014 cm^{-1} ; **MS** (MALDI)⁺ m/z 729.09($\text{C}_{43}\text{H}_{41}\text{N}_2\text{O}_7\text{P}$: [M]⁺ requires 728.77).

5.2.6 Synthesis of *N*-(2-ethylhexylamine)-*N'*-(4-aminobenzylphosphonic acid)-perylene-3,4,9,10-tetracarboxylic diimide (**PDI-2**)

PDI-1 (200 mg, 0.274 mmol) was dissolved in dry DCM (15 mL) under Ar flow. To the solution bromotrimethylsilane (0.38 mL, 2.74 mmol) was added and stirred at room temperature for 24 h. The solvent was removed by evaporation in vacuo. The solid was redissolved in a solution of MeOH/DCM (30 mL, 1:1) and stirred for 3 h. The dark red precipitate was filtered from the solution and washed with hot MeCN to leave a maroon solid (163 mg, 88%). ³¹P NMR (162 MHz, $\text{D}_2\text{O}/\text{TEA}$ (99:1)) δ 1724; **IR** (ATR): 3343, 3002, 2982, 2927, 2847, 1760, 1694, 1663, 1585, 1414, 1327, 1045 cm^{-1} ; **MS** (MALDI)⁺ m/z 673.235($\text{C}_{39}\text{H}_{33}\text{N}_2\text{O}_7\text{P}$: [M]⁺ requires 672.66).

5.3 Synthesis of Polyoxometalates

5.3.1 Synthesis of $K_6[P_2W_{18}O_{62}]$ (P_2W_{18})

Synthesis was carried out following the method described by Graham and Finke.⁶⁸

Na_2WO_4 (100 g, 340 mmol) was dissolved in deionised water (120 mL) with vigorous stirring. To the stirred solution HCl (83 mL, 4.0 M) was added dropwise via a dropping funnel at a rate of 2 drops per second resulting in the formation of a white precipitate. H_3PO_4 (83 mL, 4.0 M) was added dropwise at a rate 4 drops per second causing the white precipitate to dissolve and the solution to turn yellow. The solution was then refluxed for 24 h. After cooling the solution to room temperature KCl (50 g, 670 mmol) and vigorously stirred for 15 mins. The solution was filtered using a glass frit leaving a green chalky solid and was air dried overnight. The solid was redissolved in a minimum of boiling water and 5-6 drops of liquid bromine was added to oxidise the tungsten resulting in the solutions colour changing from green to yellow. The solution was cooled to room temperature and left to recrystallize in the fridge for 3 days. The pale-yellow crystals were collected by filtration and air dried (30.194 g, 38.7%). **³¹P NMR** (162 MHz, D_2O) δ -13.01; **IR** (ATR): 3612, 1696, 1154, 1034, 1011, 776, 542 cm^{-1} ; **MS** (ESI)⁻ m/z 2222.73 ($[P_2W_{18}O_{62}]$: $[M+Na_4]^{2-}$ requires 2222.74).

5.3.2 Synthesis of $K_{10}[P_2W_{17}O_{61}]$ (P_2W_{17})

To a stirred solution $K_6[P_2W_{18}O_{62}]$ (10 g, 2.17 mmol) dissolved in deionised water (25 mL) a solution of $KHCO_3$ (2.5 g in 40 mL of deionised water) was added resulting in a milky white suspension. Reaction was stirred for 1 h forming a white precipitate that was collected by filtration and air dried overnight. The white solid was recrystallized from a minimum volume of boiling water and left in the fridge for 3 days. The white crystals were collected by filtration and air dried (8.55 g, 86.3%). λ_{max} (abs) = 270 nm **³¹P NMR** (162 MHz, D_2O) δ -7.26, -14.34; **IR** (ATR): 3458, 1616, 1080, 798, 717, 524 cm^{-1} ; **MS** (ESI)⁻ m/z 2161.10 ($[P_2W_{17}O_{61}]$: $[M+K_4]^{2-}$ requires 2161.07).

5.3.3 Synthesis of $K_6[P_2W_{17}O_{61}(C_{39}H_{33}N_2O_5P)_2]$ (**PDI-POM**)

PDI-2 (30 mg, 0.044 mmol) was dissolved in DMA (15 mL), the solution was vigorously stirred for 15 mins. To the stirred solution $K_{10}[P_2W_{17}O_{61}]$ (100 mg, 0.022 mmol) was added and stirred for a further 5 mins. HCl (9.3 μ L, 0.264 mmol, 12 M) was added and the solution brought to 85 °C. After 18 h the dark red solution was cooled to room temperature and syringe filtered. To the filtrate Et_2O (~35 mL) was added producing a dark red precipitate which was collected by centrifugation (8000 rpm, 5 mins). The solid was dissolved in MeCN (5 mL) and centrifuged (8000 rpm, 5 mins) separating residual solid. To the supernatant Et_2O (~45 mL) was added forming a dark red precipitate that was collected by centrifugation (8000 rpm, 5 mins). The solid was redissolved in MeCN and precipitated with Et_2O two more times. The dark red solid was collected and dried (78 mg, 60.9%). λ_{max} (abs) = 526 nm; **1H NMR** (500 MHz, $D_2O/MeCN-d_3(1:1)$) δ 8.75 (s, 2H), 8.59 (s, 2H), 8.42 (s, 2H), 8.12 (s, 2H), 7.92–7.81 (m, 4H), 4.27 (s, 2H), 1.81 – 1.53 (m, 8H), 1.31 – 1.25 (t, 3H), 1.23 (t, 3H) **^{31}P NMR** (162 MHz, $MeCN-d_3$) δ 24.72, 19.80, -9.96, -10.06, -12.79, -12.93.; **IR** (ATR): 3510, 2958, 2927, 2872, 1761, 1695, 1649, 1593, 1506, 1435, 1350, 1251, 1084, 952, 912, 758, 526 cm^{-1} ; **MS** (ESI)⁻ m/z 1814.11($[P_2W_{17}O_{61}(C_{39}H_{33}N_2O_5P)_2]$: $[M+H_3]^{3-}$ requires 1814.08).

6. Bibliography

1. A. Anyushin, A. Kondinski and T. Parac-Vogt, *Chem. Soc. Rev.*, 2020, **49**, 382-432.
2. E. Hampson, J. Cameron, S. Amin, J. Kyo, J. Watts, H. Oshio and G. Newton, *Angewandte Chemie*, 2019, **58**, 182811-118285.
3. S. Omwoma, W. Chen, R. Tsunashima and Y. Song, *Coordination Chemistry Reviews*, 2014, **258**, 58-71.
4. N. Gumerova and A. Rompel, *Nature Reviews Chemistry*, 2018, **2**, 1-12.
5. A. Dolbecq, E. Dumas, C. Mayer and P. Mialane, *Chemical Reviews*, 2010, **110**, 6009–6048.
6. W. Qi and L. Wu, *Polymer International*, 2009, **58**, 1217-1225.
7. Y. Jeannin, *Chemical Reviews*, 1998, **98**, 51-76.
8. M. Bera, B. Qiao, S. Seifert, B. Burton-Pye, M. Cruz and M. Antonio, *J. Phys. Chem.*, 2016, **120**, 1317-1327.
9. A. Proust, B. Matt, R. Villanneau, G. Guillemot, P. Gouzerh and G. Izzet, *Chem. Soc. Rev.*, 2012, **41**, 7605-7622.
10. D. Long, R. Tsunashima and L. Cronin, *Angewandte Chemie International Edition*, 2010, **49**, 1736-1758.
11. B. Hasenknopf, *Frontiers in Bioscience*, 2005, **10**, 275-287.
12. L. Baker and J. Figgis, *J. Am. Chem. Soc.*, 1970, **92**, 3794-3797.
13. H. Sartzi, H. Miras, L. Vilà-Nadal, D. Long and L. Cronin, *Angewandte Chemie International Edition*, 2015, **54**, 15488-15492.
14. L. Vilà-Nadal, S. Mitchell and D. Long, *Dalton Trans.*, 2012, **41**, 2264-2271.
15. F. Zhang, W. Guan, L. Yan, Y. Zhang, M. Xu, E. Hayfron-Benjamin and Z. Su, *Inorg. Chem.*, 2011, **50**, 4967-4977.
16. R. Contant and R. Thouvenot, *Inorg. Chim. Acta*, 1993, **212**, 41–50.
17. X. Lo'pez, J. Carbo, C. Bo and J. Poblet, *Chem. Soc. Rev.*, 2012, **41**, 7537-7571.
18. R. Massart, R. Constant, J. Fruchart, J. Ciabrini and M. Fournier, *Inorg. Chem.*, 1977, **16**, 2916–2921.
19. L. Vilà-Nadal, S. Mitchell, D. Long, J. M. Poblet, S. Romo and X. Lo'pez, *Dordrecht*, 2012, 171-183.
20. R. Constant, W. Klemperer and O. Yaghi, *Inorganic Syntheses*, 1990, **27**, 104-111.
21. J. Liu, X. Zhang, Y. Li, S. Huang and G. Yang, *Coordination Chemistry Reviews*, 2020, **414**, 213260.
22. A. Proust, R. Thouvenot and P. Gouzerh, *Chemical Communications*, 2008, **16**, 1837-1852.
23. A. J. Kibler, V. S. Souza, J. A. Fernandes, W. Lewis, S. P. Argent, J. Dupont and G. N. Newton, *Frontiers in Chemistry*, 2021, **8**, 12308-12315.
24. S. Berardi, M. Carraro, A. Sartorel, G. Modugno and M. Bonchio, *Israel Journal of Chemistry*, 2011, **51**, 259-274.
25. F. Xin, M. Pope, G. Long and U. Russo, *Inorg. Chem.*, 1996, **35**, 1207-1213.
26. J. Li, R. Tan, X. Wang, E. Li, F. Zhai and S. Zhang, *Inorg. Chem. Commun.*, 2007, **10**, 216-219.
27. A. Kibler and G. Newton, *Polyhedron*, 2018, **154**, 1-20.
28. A. Hashikawa, M. Fujimoto, Y. Hayashi and H. Miyasaka, *Chem. Commun.*, 2011, **47**, 12361-12363.
29. C. Li, N. Mizuno, K. Yamaguchi and K. Suzuki, *J. Am. Chem. Soc.*, 2019, **141**, 7687-7692.
30. P. Anjali, N. Nilesh, S. Sukriti and P. Soyeb, *Science and Engineering*, 2016, **58**, 337-370.
31. M. Boujtita, J. Boixel, E. Blart, C. Mayer and F. Odobel, *Polyhedron*, 2008, **27**, 688-692.
32. A. Harriman, K. J. Elliott, M. A. H. Alamiry, L. Le Pleux, M. Se' verac, Y. Pellegrin, E. Blart, C. Fosse, C. Cannizzo, C. Mayer and O. Odobel, *J. Phys. Chem.*, 2009, **113**, 5834-5842.
33. J. Borrás-Almenar, E. Coronado, A. Müller and M. Pope, *Springer Netherlands*, 2003, **98**, 3-31.

34. C. Streb, *Dalton Trans*, 2012, **41**, 1651-1659.
35. A. Cherevan, S. Nandan, I. Roger, R. Liu, C. Streb and D. Ede, *Advanced Science*, 2020, **7**, 1903511-1903519.
36. M. Pope and G. Varga, *American Chemical Society*, 1966, **5**, 1249-1254.
37. N. Gao, H. Sun, K. Dong, J. Ren, T. Duan, C. Xu and X. Qu, *Nature Communications*, 2014, **5**, 3422.
38. Y. Ren, M. Wang, X. Chen, B. Yue and H. He, *Materials*, 2015, **8**, 1545-1567.
39. K. Kamata and K. Sugahara, *Catalyst*, 2017, **7**, 345-352.
40. S. Wang and G. Yang, *Chem. Rev.*, 2015, **115**, 4893-4962.
41. N. Fay, V. Hultgen, A. Wedd, T. Keyes, R. Forster, D. Leane and A. Bond, *Dalton Trans*, 2006, 4218-4227.
42. J. Walsh, A. Bond, R. Forster and T. Keyes, *Coordination Chemistry Reviews*, 2016, **306**, 217-234.
43. J. Cameron, D. Wales and G. Newton, *Dalton Trans*, 2018, **15**, 5120-5136.
44. L. Zhang, Y. Gong, Q. Hu, L. Wang, J. Wu and L. Yu, *J. Phys. Chem*, 2021, **125**, 1441-1446.
45. M. Li, S. Lv, M. You and M. Lin, *Cryst. Growth Des*, 2021, **21**, 4738-4747.
46. M. Bonchio, M. Carraro, G. Scorrano and A. Bagnò, *Synthesis and Catalysis*, 2004, **346**, 648-654.
47. F. Odobel, M. Séverac, Y. Pellegrin, E. Blart, C. Fosse, C. Cannizzo, C. R. Mayer, K. J. Elliott and A. Harriman, *Chem. Eur*, 2009, **15**, 3130-3138.
48. W. Herbst and K. Hunger, *Angewandte Chemie*, 2004, **116**, 4493-4494.
49. P. Kazmaier and R. Hoffmann, *J. Am. Chem. Soc*, 1994, **116**, 9684-9691.
50. C. Huang, S. Barlow and S. R. Marder, *J. Org. Chem.*, 2011, **76**, 2386-2407.
51. J. Qu, J. Zhang, C. Grimsdale and K. Mullen, *Macromolecules*, 2004, **37**, 8297-8306.
52. M. Sun, K. Mullen and M. Yin, *Chem. Soc. Rev*, 2016, **45**, 1513-1528.
53. H. Langhals, *Heterocycles*, 1995, **40**, 477-500.
54. F. Wurthner, *Chem, Commun*, 2004, **14**, 1564-1579.
55. F. Zhang, Y. Ma, Y. Chi, H. Yu, Y. Li, T. Jiang, X. Wei and J. Shi, *Scientific Reports*, 2018, **8**, 8208-8211.
56. M. Farooqi, M. Penick, J. Burch, G. Negrete and L. Brancalion, *Spectrochim. Acta A*, 2016, **153**, 124-131.
57. A. Segalina, J. Cerezo, G. Prampolini, F. Santoro and M. Pastore, *J. Chem. Theory Comput*, 2020, **16**, 7061-7077.
58. H. Zhao, Y. Zhang, H. Xu, Z. He and Z. Zhang, *Tetrahedron*, 2015, **71**, 7752-7757.
59. S. Baysec, A. Unlu, Y. Hacıoglu, Y. Udum and A. Cirpan, *Journal of Macromolecular Science*, 2015, **52**, 1-9.
60. M. J. Ahrens, M. J. Fuller and M. R. Wasielewski, *Chem. Mater.*, 2003, **15**, 2684-2686.
61. Y. Huang, S. Zhang, G. Zhong, C. Li, Z. Liu and D. Jin, *Phys. Chem*, 2018, **20**, 19037-19044.
62. J. Schill, S. Dun, M. Pouderoijen, H. Janssen, L. Milroy and A. Schenning, *Chemistry*, 2018, **24**, 7734-7741.
63. G. Ganesamoorthy, R. Vijayaraghavana and S. Pachagounder, *J. Sci. Adv. Mater. Devices*, 2018, **3**, 99-106.
64. J. Naidu, Y. Bae, K. Jeong, S. Shin and M. Lee, *Bull. Korean Chem. Soc*, 2009, **30**, 224-227.
65. S. Chai, S. Wen and K. Han, *Organic Electronics*, 2011, **12**, 1806-1814.
66. F. Wurthner, *Pure Appl. Chem.*, 2006, **78**, 2341-2349.
67. H. Miras, L. Vilà-Nadal and L. Cronin, *Chem. Soc. Rev*, 2014, **43**, 5679-5699.
68. C. Graham and R. Finke, *Inorg. Chem.*, 2007, **47**, 3679-3686.
69. C. Xue, R. Sun, R. Annab, D. Abadi and S. Jin, *Tetrahedron Letters*, 2009, **50**, 853-856.
70. A. El-Aneed, A. Cohen and J. Banoub, *Applied Spectroscopy Reviews* 2009, **44**, 210-230.
71. V. Penicaud, F. Odobel and B. Bujoli, *Tetrahedron*, 1998, **39**, 3689-3692.
72. K. Blazewska, *J. Org. Chem.*, 2014, **79**, 408-412.

73. S. Fujimoto, J. Cameron, R. Wei, K. Kastner, D. Robinson, V. Sans, G. Newton and H. Oshio, *Inorg. Chem.*, 2017, **56**, 12169–12177.
74. V. Sivamurugan, J. Grazulevicius, V. Gaidelis and s. Valiyaveetil, *Journal of Materials Chemistry*, 2009, **19**, 4268-4275.
75. J. Choi, T. Kang, Y. Bang, J. Lee, J. Song and I. Song, *Catalysis Communications*, 2015, **65**, 66-71.
76. F. Hajizadeh, F. Zonoz, S. Duval, B. Maleki and A. Amiri, *Journal of Molecular Structure*, 2021, **1224**, 129003.
77. N. Elgrishi, K. Rountree, B. McCarthy, E. Rountree, T. Eisenhart and J. Dempsey, *Journal of Chemical Education*, 2018, **95**, 197-206.
78. N. Neghmouche, A. Khelef and T. Lanez, *Journal of Fundamental and Applied Science*, 2009, **1**, 23-30.
79. S. Lee, Y. Zu, A. Herrmann, Y. Geerts, K. Mullen and A. Bard, *J. Am. Chem. Soc.*, 1999, **121**, 3513-3520.